

1 **Digital dissection of the model organism *Xenopus laevis* using contrast-enhanced**
2 **computed tomography**

3

4 Laura B. Porro^{1*} and Christopher T. Richards¹

5

6 ¹Structure and Motion Laboratory, Department of Comparative Biomedical Sciences, Royal
7 Veterinary College, Hatfield, Hertfordshire, AL9 7TA, United Kingdom

8

9 *corresponding author (lporro@rvc.ac.uk)

10

11 RH: Digital dissection of *Xenopus*

12 **Abstract**

13 The African clawed frog, *Xenopus laevis*, is one of the most widely used model organisms in
14 biological research. However, the most recent anatomical description of *X. laevis* was
15 produced nearly a century ago. Compared to other anurans, pipid frogs – including *X. laevis*
16 – exhibit numerous unusual morphological features; thus, anatomical descriptions of more
17 “typical” frogs do not detail many aspects of *X. laevis* skeletal and soft-tissue morphology.
18 The relatively new method of using iodine-based agents to stain soft tissues prior to high-
19 resolution X-ray imaging has several advantages over gross dissection, such as enabling
20 dissection of very small and fragile specimens, and preserving the three-dimensional
21 topology of anatomical structures. Here, we use contrast-enhanced computed tomography to
22 produce a high-resolution three-dimensional digital dissection of a postmetamorphic *X.*
23 *laevis* to successfully visualize: skeletal and muscular anatomy; the nervous, respiratory,
24 digestive, excretory and reproductive systems; and the major sense organs. Our digital
25 dissection updates and supplements previous anatomical descriptions of this key model
26 organism and we present the three-dimensional data as interactive portable document
27 format (PDF) files that are easily accessible and freely available for research and
28 educational purposes. The data presented here hold enormous potential for applications
29 beyond descriptive purposes, particularly for biological researchers using this taxon as a
30 model organism, comparative anatomy and biomechanical modelling.

31

107 **Key words:** frog; Anura; amphibians; CT-scanning; anatomy; iodine-potassium iodide; 3D
108 visualization.

109

110 **Introduction**

111 The African clawed frog, *Xenopus laevis* Daudin, 1802, is one of the most widely used
112 organisms in biological research, including applications in cell and molecular biology,
113 genetics, physiology, embryology, development and morphogenesis, neuroscience,
114 biomechanics, toxicology and medicine (Gurdon et al. 1971; Gurdon & Hopwood, 2000;
115 Burggren & Warburton, 2007; Wheeler & Brändli, 2009; Harland & Grainger, 2011; Clemente
116 & Richards, 2013; Richards & Clemente, 2013; Robovská-Havelková et al. 2014; Burgess,
117 2016). *Xenopus laevis* is easy to house and maintain, and its eggs and embryos are large,
118 tolerate manipulation and are produced in large quantities (Wheeler & Brändli, 2009). The
119 closely-related *X. tropicalis* was the first amphibian to have its genome fully sequenced
120 (Hellsten et al. 2010) and *X. laevis* was the first vertebrate to be successfully cloned (Gurdon
121 et al. 1958). Recently, the tetraploid genome of *X. laevis* was successfully sequenced
122 (Session et al. 2016), making *X. laevis* one of the most valuable model organisms for testing
123 complex biological hypotheses.

124 Surprisingly, given *X. laevis*' ubiquitous use and importance in biological research, its
125 anatomy is incompletely known. The most recent monographical description of *X. laevis* was
126 nearly a century ago (Grobbelaar, 1924). Subsequently, certain anatomical regions have
127 been described in varying levels of detail, including the: pelvic and proximal hind limb
128 skeleton and musculature (Green, 1931; Dunlap, 1960; Palmer, 1960; Emerson, 1982; Van
129 Dijk, 2002; Ročková & Roček, 2005; Příkryl et al. 2009); pectoral skeleton (Robovská-
130 Havelková, 2010); abdominal wall (Ryke, 1953); and head skeleton and musculature
131 (Paterson, 1939; Trueb & Hanken, 1992; Roček, 1993; Smirnov, 1994; Haas, 2001;
132 Ziermann & Olsson, 2007; Gross & Hanken, 2008; Ziermann & Diogo, 2014), particularly
133 with regards to development. Excellent dissection guides for frogs are available (Minkoff,
134 1975), including the classic work by Ecker (1889) that uses several species of the

135 neobatrachid *Rana* as the basis for anuran anatomy. However, members of the family
136 Pipidae (including *X. laevis*), which occupy a basal position within Anura (Pyron & Wiens,
137 2011), exhibit a secondarily aquatic adult lifestyle and numerous autapomorphies compared
138 to other anurans (Cannatella & Trueb, 1988; Cannatella & de Sá, 1993), including loss of the
139 tongue and vocal cords, retention of the lateral line and greatly enlarged otic capsules,
140 among many others (discussed below). Thus, anatomical descriptions of more “typical” frogs
141 do not detail many aspects of *X. laevis* skeletal and soft-tissue morphology. Additionally, the
142 anatomical nomenclature used by Grobbelaar (1924) differs from the terminology used by
143 Ecker (1889) and other more recent publications.

144 Despite the vast utility of gross dissection in understanding and teaching anatomy
145 (and the frequent use of frogs to introduce students to dissection methods), this centuries-
146 old practice is destructive and may be unsuitable for very small or delicate specimens.
147 Recent methods employing radiographic contrast agents, particularly iodine-potassium
148 iodide (I₂KI), alongside microcomputed tomography (μ CT) permit visualization of soft tissues
149 in high-resolution (Metscher, 2009a,b; Jeffery et al. 2011; Gignac et al. 2016). Diffusible
150 iodine-based contrast-enhanced μ CT (diceCT, *sensu* Gignac et al. 2016) has been used to
151 produce digital dissections of many post-embryonic vertebrates, particularly the heads of fish
152 (Metscher, 2013; Kleinteich, 2014; Brocklehurst et al. in prep), crocodylians (Tsai & Holliday,
153 2011; Holliday et al. 2013), birds (Düring et al. 2013; Lautenschlager et al. 2013; Qualye et
154 al. 2014) and mammals (Cox & Jeffery, 2011; Hautier et al. 2012; Cox & Faulkes, 2014), as
155 well as amphibian tongues (Kleinteich & Gorb, 2015a,b). Digital dissection via diceCT can be
156 used to visualize very small or delicate soft-tissue structures, and structures deep to skeletal
157 elements that are difficult to access via gross dissection. Simultaneously, diceCT precisely
158 reveals the rich and intricate 3D topological relationships between the skeleton and soft-
159 tissue structures. In addition to being used to illustrate anatomy for descriptive purposes,
160 segmentation of these μ CT datasets can be used to create interactive 3D reconstructions
161 (including 3D PDFs) that can be easily accessed by students and the general public. Finally,
162 3D reconstructions can be utilized by researchers interested in comparative anatomy,
163 taxonomy and cladistics, and can serve as the basis for biomechanical analysis, including
164 musculoskeletal modelling (Kargo et al. 2002) and finite element analysis (Holliday et al.
165 2013; Gignac et al. 2016).

166 We used diceCT to produce a high-resolution digital dissection of the model
167 organism *X. laevis*, supplementing and updating previous descriptions. We focus on
168 musculoskeletal anatomy, although our dissection also reveals the nervous, respiratory,
169 digestive, excretory and reproductive systems, as well as the major sense organs. As in
170 Holliday et al. (2013), we intend this contribution to serve as a visual atlas rather than a
171 structure-by-structure verbal description of *Xenopus* anatomy, although we highlight features
172 that differ radically in *X. laevis* compared to other frogs and attempt to resolve discrepancies
173 in the identification and nomenclature from previous publications. We emphasize that the 3D
174 reconstruction (including its specific geometry) *is* our hypothesis regarding the anatomy of *X.*
175 *laevis* and should be referred to for further details.

176

177 **Methods**

178 A deceased post-metamorphic male specimen of *X. laevis* (snout-vent length [SVL]: 18.38
179 mm; body mass [BM]: 0.64 g) was obtained from an unrelated study and not collected for the
180 purpose of this research; thus, animal care protocols are not required. The specimen was
181 fixed in a 4% phosphate-buffered paraformaldehyde solution. All μ CT-scanning was carried
182 out at the Cambridge Biotomography Centre (Zoology Department) at the University of

183 Cambridge in 2015 on an X-Tek H 225 μ CT scanner (Nikon Metrology, Tring, UK). All
184 specimens were scanned using a tungsten target, a background medium of air, no filter and
185 were rendered as 16-bit TIFFs. The specimen of *X. laevis* was μ CT-scanned prior to staining
186 at 68 kV and 350 μ A producing 1409 TIFF images at a resolution of 0.019 mm/voxel (Fig.
187 1A, C, E) – voxels were isometric for all scans. Subsequently, the specimen was stained in a
188 solution of 3.75% weight-by-volume I₂KI in for approximately 60 hours; the solution was
189 neither refreshed nor agitated during staining. Following staining, the specimen was μ CT-
190 scanned again at 72kV and 290 μ A producing 1490 TIFF images at a resolution of 0.017
191 mm/voxel (Fig. 1B, D, F). An unstained specimen of *Kassina maculata* (the red-legged
192 running frog, SVL: 45.10 mm; BM: 13.68 g) was μ CT-scanned at 65 kV and 340 μ A
193 producing 1158 TIFF images at a resolution 0.0493 mm/voxel. *Kassina maculata* is a
194 derived hyperoliid frog (nested within Neobatrachia and Ranoides, Pyron & Wiens, 2011)
195 that thrives in varying terrain and is capable of jumping, running, climbing and swimming
196 (Ahn et al. 2004; Porro et al. Accepted); this contrasts with the more basally-positioned and
197 almost exclusively aquatic *X. laevis*. Scan data from *K. maculata* were included to compare
198 the unusual osteology of *X. laevis* with that of a taxon possessing a skeletal morphology and
199 locomotor modes more typical of anurans.

200 Scan data was segmented in the visualization software Avizo 8.0 (FEI, Oregon,
201 USA). Density thresholding was used to separate higher-density bone from lower-density
202 soft-tissues in unstained data sets, and then processed slice-by-slice (interpolating across
203 no more than 5 slices) to separate individual bones. The stained data set of *X. laevis* was
204 manually segmented to isolate individual soft tissues from each other. The dynamic
205 histogram slider in Avizo was adjusted to enhance contrast between soft tissues. Anatomical
206 structures were delineated using overall morphology, variations in density (e.g., nervous
207 tissue was denser [brighter] than muscle, connective tissues separating muscles were less
208 dense [darker] than surrounding muscle), and structural variations (e.g., differences in fiber
209 orientation between adjacent muscles). Unstained and stained data sets of *X. laevis* were
210 overlain using recognizable skeletal landmarks visible in both data sets and merged to
211 create anatomical reconstructions. Three-dimensional surfaces were exported as wavefront
212 (OBJ) files to create interactive 3D PDFs using Tetra4D Reviewer and Converter (Tech Soft
213 3D, Oregon, USA) and Adobe Acrobat Pro X (Adobe Systems Inc., California, USA) ,
214 following methods described by Lautenschlager & Ruecklin (2014). These reconstructions
215 are provided as Supplemental Material (Figs. S1 – S4) and are the basis for the following
216 description.

217

218 **Results**

219

220 Osteology

221 The skeletal anatomy of frogs, including *X. laevis*, has been extensively described (Ecker,
222 1889; Trueb & Hanken, 1992). Comparing the skull osteology of *X. laevis* and *K. maculata*
223 (Fig. 2) highlights numerous autapomorphies of Pipidae, including: elongate septomaxillae;
224 azygous frontoparietals; loss of the quadratojugal; flattening of the posterior and medial rami
225 of the pterygoid; and loss of the mentomeckelian of the lower jaw (Cannatella & Trueb, 1988;
226 Smirnov, 1994). The squamosal is modified into a funnel-shaped structure (unique to pipids)
227 that houses the columnella and its anterior process articulates with pterygoid (unique to
228 *Xenopus* and *Silurana*). *Xenopus* is a neotenic frog in which development continues after
229 sexual maturation (Smirnov, 1994). Our digital dissection of a young individual underscores
230 features of *Xenopus* cranial morphology that vary during ontogeny. In our specimen: the

231 nasals are separate (they fuse in older animals) while the vomers are azygous (they are
232 paired in older animals); the palatine is absent (it appears in older individuals); the maxilla
233 lacks a preorbital process and the parasphenoid lacks lateral alae (both appear in animals
234 over 12 years old) (Cannatella & Trueb, 1988; Smirnov, 1994).

235 Unusual features in the postcranial skeleton of *X. laevis* compared to neobatrachians
236 (Fig. 3, supplementary PDF S1) include fusion of the sacrum and urostyle, unique ridging on
237 the ilia and urostyle, absence of the omosternum, fusion of the clavicle and scapula, and
238 presence of a cartilaginous praepubis/epipubis (Cannatella & Trueb, 1988; Reilly and
239 Jorgensen, 2011). Pronounced differences in pelvic morphology – including overall shape,
240 and the nature of the sacroiliac and sacrourostylic articulations – among anuran taxa have
241 been linked to divergent locomotor behaviours (e.g., predominantly swimming in *X. laevis*)
242 (Whiting, 1961; Emerson, 1979, 1982; Reilly & Jorgensen, 2011).

243

244 Musculature

245 Details of muscle origins and insertions are described in Table 1 and presented in
246 supplementary PDF S2.

247

248 *Head and throat musculature*

249 We use the nomenclature of Ziermann & Diogo (2014) to label and describe anuran head
250 musculature; however, the terminology for the cranial muscles in anurans varies even
251 among recent publications (Hass, 2001; Johnston, 2011). The orbital musculature (Fig. 4A –
252 C) is composed of six extrinsic muscles: the four *rectus* muscles, which originate from the
253 posteromedial corner of the orbit and surround the optic nerve (CN II); and the two *obliquus*
254 muscles, which originate from the anteromedial corner of the orbit. The three portions of *M.*
255 *retractor bulbi* are surrounded by the cone formed by the *rectus* muscles, and *M. levator*
256 *bulbi* forms the floor of the orbital cavity (Fig. 4C). The jaw elevators (Fig. 4D – F) are
257 identified by their attachment sites and relationships to the mandibular branch of the
258 trigeminal nerve (CN V₃). Ziermann & Diogo (2014) divide *M. adductor mandibulae* A2
259 (identified in older publications as the masseter) into A2 and A2 *lateralis* portions; however,
260 separate muscle bodies cannot be visualized in our μ CT data. Fusion of *M. adductor*
261 *mandibulae* A2 PVM (posteroventromesial) and A3' creates the muscle widely known as the
262 temporalis, which is separated from the deeper A3'' (pterygoideus) by CN V₃. A
263 synapomorphy of Pipidae is the division of the *M. depressor mandibulae*, the primary jaw
264 opener, into two parts (Cannatella & Trueb, 1988); the separate origins of the larger and
265 smaller portions dorsal and ventral to *M. cucullaris*, respectively, are visible in our μ CT data
266 (Fig. 4E).

267 As *Xenopus* lacks a tongue, the hyoid musculature is highly unusual (Fig. 4G, H): *M.*
268 *hypoglossus*, *M. genioglossus* (Grobelaar, 1924; Ziermann & Diogo, 2014) and portions of
269 *M. petrohyoideus* (see below) are absent. The *M. intermandibularis anterior* and *posterior*
270 (widely known as the submentalis and submaxillaris/mylohyoideus, respectively) form the
271 floor of the oral cavity and underlie all other throat muscles; a robust posterior slip of *M.*
272 *intermandibularis posterior* originates on the ventral margin of the lateral edge of the
273 pterygoid and anteroventral margin of the prootic, and is likely the muscle referred to as the
274 *M. subhyoideus* by Grobelaar (1924) and figured by Ecker (1889) (Fig. 4G). The paired *M.*
275 *geniohyoideus* muscles are well-developed and each divides posteriorly into medial and
276 lateral portions. *M. sternohyoideus* is an anterior continuation of *M. rectus abdominis* (see
277 below); it originates external to *M. rectus abdominis* at the level of the clavicle (Ryke, 1953),
278 and is visible between the lateral and medial portions of *M. geniohyoideus*. The status of *M.*

279 *omohyoideus* in *Xenopus* is unclear – Grobbelaar (1924) states this muscle is absent. In
280 contrast, Ziermann & Diogo (2014) state *M. omohyoideus* is present in adult *Xenopus* and
281 courses from the sternum to the hyoid; however, the typical origin of *M. omohyoideus* is on
282 the anterior margin of the scapula (Ecker, 1889). An anterior slip of what we identify as *M.*
283 *sternoradialis* may represent *M. omohyoideus* in our specimen. Frogs typically possess a
284 single *M. petrohyoideus anterior* and three slips representing *M. petrohyoideus posterior*
285 (Ecker, 1889); only one slip is present in *Xenopus* (Grobbelaar, 1924; Ziermann & Diogo,
286 2014), representing the posterior (third) slip of *M. petrohyoideus posterior*.

287

288 *Back and abdominal musculature*

289 Back muscles attaching to the pectoral girdle or forelimbs are discussed below. The back
290 muscles of all frogs are externally (dorsally) covered by an extensive *fascia dorsalis* that
291 attaches to the frontoparietal bone of the skull and spinous processes of the vertebrae
292 (Ecker, 1889); in *Xenopus*, the posterior portion of *fascia dorsalis* thickens to become a
293 ligamentous plate extending between the iliac shafts (Fig. 5A, E; Prikryl et al. 2009). The
294 most prominent back muscle is *M. longissimus dorsi*, which extends from anterior half of the
295 urostyle to the occiput (Fig. 5A, D, E). *M. coccygeosacralis* is absent in *Xenopus*
296 (Grobbelaar, 1924; Prikryl et al. 2009); *M. coccygeoiliacus* originates along the urostyle and
297 passes ventral to the sacrum to insert on the medial aspect of the ilium (Fig. 5B, E). There
298 are two origins for *M. iliolumbaris* as identified by Ryke (1953) and Palmer (1960); the bulk of
299 the muscle originates from the ventral aspects of the presacral vertebrae with one small slip
300 originating on the tip of the 4th rib (Fig. 5 B, D). Our digital dissection demonstrates *M.*
301 *iliolumbaris* originates further anteriorly than previously described by some authors (but
302 similar to Whiting [1961]), and may explain the extension of the iliac shafts far beyond the
303 anterior margins of the sacrum (Ročková & Roček, 2005). The *M. intertransversarii* between
304 adjacent transverse processes are clear but the *M. intercrurales* cannot be visualized in our
305 specimen; however, Grobbelaar (1924) claims these two muscle masses are merged. Both
306 *M. intertransversarius capitis superior* and *inferior* arise from the second transverse process
307 and insert on the prootic-exoccipital complex (Fig. 5B).

308 In addition to work by Grobbelaar (1924), Ryke (1953) described the development of
309 the trunk musculature of *Xenopus* during metamorphosis. *M. obliquus externus* is the most
310 superficial abdominal muscle (although much of it is covered by *M. latissimus dorsi* and the
311 abdominal portion of *M. pectoralis*, see Fig. 5A and below). A small slip representing *pars*
312 *scapularis* of *M. obliquus externus* inserts between *M. serratus inferior* and *M. latissimus*
313 *dorsi*; however, whether it ultimately inserts on the posterior margin of the scapula or
314 suprascapula is unclear (Ecker, 1889; Grobbelaar, 1924; Ryke, 1953). The dorsal margin of
315 *M. transversus abdominis* (which has merged with *M. obliquus internus* in frogs see Ecker
316 [1889]) is externally overlapped by the ventral margin of *M. obliquus externus*; its
317 anteroventral margin externally overlaps the dorsal margin of the deeper *M. rectus*
318 *abdominis* (Fig. 5C, D, E). As noted by Ryke (1953), posterior portions of *M. obliquus*
319 *externus* and *M. transversus abdominis* merge in post-metamorphic *Xenopus* while the
320 anteroventral fibres of *M. transversus abdominis* are indistinguishable from those of *M.*
321 *rectus abdominis profundus* (Ecker, 1889; Ryke, 1953). The deep surface of *M. transversus*
322 *abdominis* contacts several of the internal organs, particularly the lungs and liver (Ryke,
323 1953). *M. rectus abdominis* is divided into deep and superficial layers. *M. rectus abdominis*
324 *profundus* forms the deepest layer of the abdominal musculature (Fig. 5C, D, E); it arises
325 from the epipubis and longitudinally spans the ventral aspect of the abdomen on either side
326 of the midline (Fig. 5C). Anteriorly, some fibres insert on the clavicle but most continue

327 anteriorly as *M. sternohyoideus*. The posterior fibres of *M. rectus abdominis superficialis* in
328 post-metamorphic *Xenopus* are indistinguishable from those of *M. rectus abdominis*
329 *profundus* (Ryke, 1953). Anteriorly, its fibres follow and are closely associated with those of
330 *M. pectoralis* (Fig. 5C), and insert on the scapula as described by Ecker (1889) and not on
331 the sternum, contrary to descriptions by Grobbelaar (1924) and Ryke (1953).

332

333 *Pectoral and forelimb musculature*

334 As with the cranial musculature, the nomenclature for the muscles of the pectoral girdle and
335 forelimb varies throughout the literature (Diogo & Ziermann, 2014). Several major pectoral
336 muscles originate on the skull and vertebral column (Figs. 5 and 6). The largest and most
337 superficial of the dorsal pectoral muscles is *M. latissimus dorsi* (Figs. 5A and 6A, G, H).
338 *Xenopus* is unusual among anurans in that this muscle laterally overlaps the suprascapula
339 and extends posteriorly to cover the anterior tips of the ilia (Grobbelaar, 1924; Přikryl et al.,
340 2009). Mason et al. (2009) describe *M. cucullaris* as originating on the stapes, otic capsule
341 and tympanic annulus in *X. laevis* (Fig. 6A, G), similar to descriptions and illustrations by
342 Grobbelaar (1924) and Minkoff (1975); in contrast, Ecker (1889) describes and illustrates *M.*
343 *cucullaris* arising from the posterodorsal aspect of the skull. This muscle is, in fact, *M.*
344 *rhomboideus anterior* (Fig. 6A, G, Grobbelaar, 1924) and the muscle labeled and described
345 as *M. sternocleidomastoideus* by Ecker (1889) is the *M. cucullaris* of Grobbelaar (1924) and
346 Mason et al. (2009). Minkoff (1975) claims *M. cucullaris* and *M. sternocleidomastoideus* are
347 synonymous; this appears to be the case as we could not identify a separate *M.*
348 *sternocleidomastoideus* in our data set. The *M. levator scapulae superior* (Fig. 6B, G, H) of
349 later authors (Grobbelaar, 1924; Mason et al. 2009) appears to be equivalent to the *M.*
350 *protrahens scapulae* of Ecker (1889), and the *M. levator scapulae inferior* (Fig. 6B, H) of
351 Grobbelaar (1924) is equivalent to the *M. levator anguli scapulae* of Ecker (1889). The *M.*
352 *serratus superior*, *M. serratus medius* and *M. serratus inferior* (Fig. 6C, H) of Grobbelaar
353 (1924) are equivalent to the *M. transverso-scapularis tertius* s. *serratus*, *M. transverso-*
354 *scapularis minor* and *M. transverso-scapularis major*, respectively, of Ecker (1889).
355 Furthermore, Ecker (1889) describes an additional muscle (*M. retrahens scapulae*) with
356 attachments identical to *M. serratus inferior*, and raises the possibility that the two may
357 represent a single muscle; no separate *M. retrahens scapulae* was found in our specimen.

358 The ventral aspect of the posterior pectoral region is dominated by the *M. pectoralis*
359 *pars abdominalis* (Figs. 5C, 6D). *M. pectoralis pars sternalis anterior* and *M. pectoralis pars*
360 *sternalis posterior* (Fig. 6D) of Ecker (1889) are equivalent to *M. mylo-pectori-humeralis*, *M.*
361 *supracoracoideus* and *M. sternocoracoideus* of Grobbelaar (1924). The proximal portions of
362 *M. sternoradialis* (*M. coraco-radialis* of Grobbelaar, 1924) and *M. coracohumeralis* (*M.*
363 *coraco-brachialis* of Grobbelaar, 1924) are very difficult to separate in our data set although
364 their distal insertions on the forelimb are distinct (Fig. 6D, G). The *M. scapulo-humeralis*
365 *profundus anterior* of Grobbelaar (1924) appears to be equivalent to *M. subscapularis* (Fig.
366 6E, H, J). However, our data set reveals a small muscle that Grobbelaar (1924) terms the *M.*
367 *scapulo-humeralis profundus posterior*; this muscle is either absent or microscopic in most
368 anurans (Fig. 6E, G). The external surface of the shoulder is covered by *M. dorsalis*
369 *scapulae* (*M. infraspinalis* of Grobbelaar, 1924) and three heads of *M. triceps brachii* (long,
370 lateral and medial) are distinct in our scans (Fig. 6E, H – K); however, the fourth head (deep
371 [Grobbelaar, 1924], *anconeus* [Minkoff, 1975], *subanconeus* [Ecker, 1889]) cannot be
372 resolved in our data set. An unknown muscle stretches between the internal aspect of the
373 scapula and the distal tip of the coracoid (Fig. 6E).

374 Resolution of the flexor compartment muscles of the forearm is generally good (Fig.
375 6I – L), and *M. flexor carpi radialis* and *ulnaris*, *M. flexor antebrachii medialis* and *M. flexor*
376 *digitorum communis* (*M. palmaris longus* of later studies [Minkoff, 1975]) are easily
377 distinguished, although *M. epitrochleocubitalis* and *M. ulnocarpalis* cannot be resolved. In
378 contrast, resolution of the muscles in the extensor compartment is poor and, with the
379 exception of *M. flexor antebrachii superficialis* and *profundus*, individual muscles in this
380 region and in the hand could not be distinguished due to the very small size of these
381 structures. Attachment sites for pectoral and forelimb muscles are shown in Fig. 7.

382

383 *Pelvic and hind limb musculature*

384 The pelvic musculature of pipids, including *Xenopus*, is radically different from that of typical
385 anurans (Figs. 8 and 9). In addition to work by Grobbelaar (1924) and Dunlap (1960), the
386 muscles of the pelvis and proximal hind limb of *Xenopus* have been more recently described
387 by Přikryl et al. (2009). Dunlap (1960) described two portions of *M. iliacus externus* in
388 *Xenopus*; our digital dissection supports the presence of at least three separate layers (Fig.
389 8A, B, H – J) as described by Grobbelaar (1924), Ryke (1953) and Přikryl et al. (2009),
390 although attachment sites vary slightly from those previously reported (Fig. 9). Additionally,
391 our digital dissection revealed a distinct separate portion of the middle layer of *M. iliacus*
392 *externus* (Figs. 8A, B and 9B IE'') originating on the ventral surface of the ligamentous plate
393 and medial aspect of the posterior iliac shaft, and sharing its insertion with the main middle
394 portion of *M. iliacus externus* (IE'). In transverse cross-section, this muscle mass is what
395 Ryke (1953, Fig. 22) incorrectly labeled as *M. coccygeosacralis*, which is fused to *M.*
396 *longissimus dorsi* in *Xenopus* (Přikryl et al., 2009). *M. pyriformis* is present and robust in our
397 specimen (Fig. 8A) *contra* suggestions by Dunlap (1960) and Přikryl et al. (2009) that it is
398 reduced or absent. The *M. epipubicus* of Grobbelaar (1924), a muscle unique to *Xenopus*,
399 could not be distinguished from the cartilaginous praepubis in our scan data.

400 The attachments of the thigh muscles of *X. laevis* are summarized in Table 1 and
401 Fig. 9. Three thigh muscles – *M. tensor fascia latae*, *M. cruralis* and *M. gluteus magnus* –
402 form what is known as the *M. triceps femoris* complex of frogs (Fig. 8C, D, J, K; Grobbelaar,
403 1924; Přikryl et al., 2009). The well-developed *M. tensor fascia latae* in our specimen has no
404 bony attachments, originating from the fascia covering *M. iliacus externus* and inserting on
405 the fascia of *M. cruralis*. Neither the division of *M. cruralis* into three heads nor the accessory
406 tendon of *M. gluteus magnus* (Grobbelaar, 1924; Dunlap, 1960) can be visualized in our
407 data. In contrast, the oblique tendinous inscriptions within *M. semimembranosus* and *M.*
408 *gracilis major* are visible (Ecker, 1889; Přikryl et al., 2009). Although the anterior margin of
409 *M. semitendinosus* and posterior margin of *M. sartorius* are closely associated in our data
410 sets (Fig. 8D, I, J), both muscles are distinct and unfused, *contra* descriptions by Grobbelaar
411 (1924), Dunlap (1960) and Přikryl et al. (2009). Only the ventral head of *M. semitendinosus*
412 is present in our specimen, as described and illustrated by Přikryl et al. (2009) for *X. laevis*.
413 The ventral and dorsal portions of *M. adductor magnus* (Fig. 8E, F, I – J) are distinct and
414 together form a muscular sheath (located between the superficial muscles of the thigh
415 described above and the deepest layers, described below) that wraps around most of the
416 femur. As noted by Dunlap (1960) and Přikryl et al. (2009), *M. adductor longus* is absent in
417 *Xenopus* because it has not separated from *M. pectineus* (Fig. 8F, I); Grobbelaar (1924)
418 describes the two muscles as being separate but in very close contact. Similarly, *M.*
419 *obturator externus* is confluent with *M. quadratus femoris* in *Xenopus* (Fig. 8I, Grobbelaar,
420 1924; Dunlap, 1960; Přikryl et al., 2009).

421 The shank muscles of *X. laevis* (Fig. 10) have been described by Dunlap (1960) and
422 were figured but not described by Grobbelaar (1924). The shank muscles are generally
423 uniform across anurans (Dunlap, 1960). In contrast, numerous foot muscles present in most
424 anurans are absent in *Xenopus*, including: *M. abductor prae hallucis*; *M. lumbricalis brevis*
425 *hallucis*; *M. opponens hallucis*; *M. flexores ossei metatarsi digitorum III* and *IV*; *M. flexores*
426 *teretes digitorum II* and *V*; *M. extensor brevis superficialis digiti V*; and *M. extensor brevis*
427 *medius digiti V*. Within the shank, our μ CT data reveals the fusion between the origins of *M.*
428 *peroneus* and *M. extensor cruris brevis* unique to *Xenopus* as well as a heavy aponeurosis
429 within *M. plantaris longus* (Fig. 10 A, B). Resolution of individual muscles becomes difficult in
430 the tarsus and foot due to the very small size of these structures. *M. tarsalis posticus* cannot
431 be distinguished from *M. plantaris profundus*, with which it shares similar attachment sites
432 (Fig. 10B, F, L). No distinction can be made between the *M. lumbricales breves*, *longus* and
433 *longissimus* in our μ CT data; the lumbricals (along with *M. abductor proprius digiti IV*) are
434 presented in our digital dissection as a single, undivided mass (Fig. 10H). Furthermore, most
435 of the very thin *M. extensores breves medii digitorum* are partially fused with *M. extensores*
436 *breves superficiales digitorum* (Dunlap, 1960); only the muscle for the second digit is distinct
437 in our data set (Fig. 10I). Several very small foot muscles cannot be resolved in our data,
438 including: the undivided *M. transversus plantae*; *M. contrahentes digitorum I, II* and *V*; *M.*
439 *flexor ossis metatarsi digiti II*; *M. flexores teretes digitorum III* and *IV*; *M. transversi metatarsi*
440 *I – IV*; and *M. extensor brevis profundus digit V*. Lastly, there is a substantial muscle along
441 the ventral aspect of metatarsal I (Fig. 10H); the position of this muscle resembles those of
442 the lumbricals in other digits. However, according to Dunlap (1960), *M. lumbricalis brevis*
443 *hallucis* is absent in *Xenopus* and thus the identity of this muscle is uncertain.

444

445 Nervous system

446 Visualization of the central nervous system and the larger peripheral nerves in our data set
447 was excellent (Fig. 11, supplementary PDF S3). The major portions of the brain – cerebral
448 hemispheres, thalamencephalon/ diencephalon, pineal body, optic lobes, hypothalamus and
449 pituitary body, cerebellum and medulla oblongata, as well as their internal ventricles – are
450 clearly visible (Fig. 11A – D). The olfactory lobes can be seen in surface renderings as
451 anterolateral swellings of the cerebral hemispheres. There is no clear distinction between the
452 medulla oblongata and spinal cord; in our reconstructions, the two are divided at the foramen
453 magnum. The spinal cord features two prominent swellings along its length (Fig. 11E) from
454 which arise the nerves of the pectoral and pelvic plexuses (Ecker, 1889). Posteriorly, the
455 spinal cord tapers abruptly to a conus medullaris and filum terminale that continues into the
456 urostyle (Fig. 11E).

457 There are ten pairs of cranial nerves in frogs (Fig. 11E, F) – the accessory (CN XI)
458 and hypoglossal (CN XII) nerves of amniotes are absent. The short olfactory nerve (CN I)
459 courses from the anteroventral aspect of the olfactory lobe to the ventromedial aspect of the
460 sphenethmoid cartilage (Fig. 11E). The optic nerves (CN II) can be traced from their chiasma
461 on the ventral aspect of the brain to the eyes. The oculomotor nerve (CN III) can be traced
462 emerging from the brain and passing through the wall of the cranium; it then passes near
463 and exchanges fibers with the ophthalmic branch of the trigeminal nerve (CN V₁), becoming
464 indistinguishable from the latter (Ecker, 1889). The trochlear nerve (CN IV), also closely
465 associated with CN V₁ (Ecker, 1889), cannot be distinguished in our data set. The largest
466 cranial nerve, the trigeminal (CN V; Fig. 11F), arises from the anterolateral aspect of the
467 medulla oblongata, passes forward to form the large Gasserian ganglion, then immediately
468 divides into the ophthalmic branch (CN V₁) – which travels between the cranium and eyeball,

469 before dividing into two terminal branches – and the maxillo-mandibular trunk. A large
470 branch – the palatine nerve – originates near the base of CN V₁ and courses along the
471 ventral aspect of the skull parallel to the midline. The maxillo-mandibular trunk passes
472 behind the eyeball, between A3' and A3'' and courses along the external surface of A3'
473 before dividing into the short maxillary branch (CN V₂) and longer mandibular branch (CN
474 V₃). The tiny abducens nerve (CN VI) originates from the ventral aspect of the medulla
475 oblongata behind the hypothalamus, joins the Gasserian ganglion and is then
476 indistinguishable from CN V₁ (Fig. 11E). The facial nerve (CN VII) can be traced from the
477 Gasserian ganglion, where it immediately divides into a short, stout palatal branch (that joins
478 the palatine nerve of CN V₁) and a much longer hyomandibular branch, which courses
479 posteriorly around the otic capsule, behind the angle of the lower jaw and then anteriorly
480 along the ventral margin of the lower jaw. The auditory or vestibulocochlear nerve (CN VIII)
481 is a short, stout nerve that passes through a foramen into the otic capsule and immediately
482 divides into a number of small nerves (Fig. 11E). The glossopharyngeal (CN IX) and vagus
483 (CN X) nerves arise and exit the skull together, and cannot be differentiated in our data set
484 (although the former joins CN VII). CN X turns posteriorly and can be traced under the skin
485 of the dorsolateral aspect of the back along the length of the body as it supplies the lateral
486 line (Fig. 11E).

487 Ten pairs of spinal nerves were identified in our data set (Fig. 11G); for each, the
488 dorsal and ventral roots and spinal ganglia are clearly visible. Only major features of these
489 nerves will be discussed here, as individual branches are detailed by Ecker (1889). The first
490 spinal nerve (also called the hypoglossal nerve, Ecker [1889]) has an extremely slender
491 dorsal root and emerges between the first and second vertebrae, giving off a series of small
492 branches before turning sharply ventrally and anteriorly. The second spinal nerve is the large
493 brachial nerve that supplies the shoulder and forelimb. The third spinal nerve is much
494 smaller and, upon exiting between the third and fourth vertebrae, almost immediately joins
495 the brachial nerve to supply the forelimb. The fourth, fifth and sixth spinal nerves are closely
496 associated with each other and supply the abdominal muscles and skin. The seventh spinal
497 nerve is large and initially follows the sciatic nerve before turning ventrally and medially,
498 sending off a number of branches to the abdominal, pelvic and thigh muscles. The sciatic
499 nerve is the largest nerve in the body and is composed primarily of the eighth and ninth
500 spinal nerves, with contributions from the seventh; it supplies the hind limb. The tenth spinal
501 nerve is extremely slender and exits the urostyle through a small lateral perforation.

502

503 Digestive system and glands

504 The digestive tract consists of the mouth, esophagus, stomach, small and large intestines,
505 and their associated glands (Fig. 12A, B, supplementary PDF S4). *Xenopus laevis* bears
506 teeth on the premaxilla and maxilla, but vomerine teeth are absent in this species (Evans et
507 al. 2015). The intermaxillary glands (Fig. 12A) are clearly visible between the anterior tip of
508 the parasphenoid and the oral margin of the mouth, and the paired internal nares (choanae)
509 open into the oral cavity immediately posterior to these glands. Further posteriorly, the left
510 and right Eustachian tubes join and open into the pharynx via a single, median opening, a
511 feature unique to pipids (Smirnov, 1994). The floor of the mouth in *X. laevis* is marked by the
512 absence of a tongue.

513 There is no clear distinction between the end of the oral cavity and the esophagus,
514 which lies dorsal to the larynx. The esophagus (Fig. 12A, B) is a nearly straight tube that is
515 largest (and dorsoventrally flattened) anteriorly and tapers to a rounded cross section near
516 its junction with the stomach. Scans reveal the tight folds of the mucosal and muscular

517 layers of the esophagus becoming increasingly convoluted as it approaches the stomach.
518 The junction between the esophagus and stomach is marked by a strong curve to the left, a
519 marked increase in the diameter of the tube and noticeably thicker walls. The stomach (Fig.
520 12A, B) is kidney-shaped and high density particles visible in within it (and the large
521 intestine) in μ CT scans are the remains of food. The stomach terminates by curving upwards
522 and towards the right; a marked constriction marks the beginning of the long, coiling small
523 intestine (Fig. 12A). Initially, the walls of the small intestine are thinner and exhibit less
524 folding than those of the stomach. The walls become increasingly convoluted in the middle
525 of the small intestine before once again thinning, with less pronounced folding in the walls as
526 it approaches its junction with the large intestine. A sharp ventral curve and increase in
527 diameter mark the beginning of the large intestine (Fig. 12A, B), which is initially very wide
528 and thin-walled. The large intestine tapers abruptly as it passes between the ilia and ischia
529 and opens into the cloaca dorsal to the opening of the bladder.

530 There are three distinct lobes of the liver, which occupy the anteroventral portion of
531 the abdomen (Fig. 12A, B). All lobes are ventrally and anteriorly convex (domed) and
532 dorsally concave. The left lobe is largest and covers the anteroventral surfaces of the
533 stomach and left lung. The right lobe extends anterior to the left lobe, covers the
534 anteroventral aspect of the right lung and is joined to the small median lobe, which lies
535 posterior to the apex of the heart and overlaps the ventral aspect of the distal esophagus.
536 The small, round gallbladder (Fig. 12A) lies between the left and median lobes, and is
537 connected to the lobes of the liver by a series of hepatic and cystic ducts. The common bile
538 duct from the gallbladder to the duodenum of the small intestine courses along the entire
539 medial (right) border of the pancreas. The glandular pancreas (Fig. 12A) is flattened in
540 cross-section and occupies a loop formed by the distal end of the esophagus, the stomach
541 and the duodenum.

542 The spleen (part of the lymphatic system, but described here as an abdominal organ)
543 is a radio-dense, small, round organ located on the right side of the abdomen within the
544 curve formed by the large intestine and ventrally overlapped by the small intestine (Fig. 12A,
545 B). The thymus glands (Fig. 12A) are small, circular bodies located on the sides of the head
546 between *M. depressor mandibulae* and *M. latissimus dorsi* and the oval-shaped thyroid
547 glands (Fig. 12A) are located between the *M. sternohyoideus* and the anterior tip of the
548 larynx.

549

550 Urogenital system

551 The paired kidneys (Fig. 12B, supplementary PDF S4) are elongate organs located ventral
552 to the vertebrae and dorsal to the other abdominal organs, and extend from the fifth vertebra
553 to the posterior end of the ilia. The ureters (Fig. 12B) are visible at the distal ends of the
554 kidney. The urinary bladder (Fig. 12A) is bilobate (as in all amphibians), thin-walled and lies
555 against the ventral aspect of the large intestine, opening into the cloaca ventral to the
556 opening of the digestive tract. The individual we scanned possesses a pair of small, elongate
557 organs located on the ventromedial aspect of the kidneys, approximately one-third from their
558 anterior ends (Fig. 12B), which are testes and identify this young individual as a male. The
559 adrenal glands could not be located and no fat bodies were present.

560

561 Respiratory and circulatory systems

562 The respiratory tract consists of the larynx and lungs (Fig. 12C, supplementary PDF S4).
563 The larynx is a funnel-shaped tube with its apex pointed anteriorly; it lies in the midline
564 ventral to the esophagus, between the thyrohyals. The anterior end is a thin tapered tube

565 that opens into the floor of the mouth via a longitudinal slit (glottis); posteriorly, a pair of short
566 bronchi open into the lungs. The larynx is sexually dimorphic in *X. laevis*, and its shape in
567 this specimen (as well as restriction of the *M. dilator laryngis* muscle to the lateral surfaces of
568 the larynx) more closely resembles the female condition than that of the male (Sassoon &
569 Kelley, 1986); this is due to the young age of this individual. The lungs are thin-walled and
570 tear-drop shaped, tapering toward their posterior ends. They are located dorsal to the organs
571 of the digestive tract and the left lung extends posteriorly beyond the right lung.

572 Although our methods produced excellent resolution of the muscles, internal organs
573 and nervous system, visualization of the circulatory system was poor. The heart and the
574 major vessels leading from the heart were over-stained, whereas the peripheral circulatory
575 system did not stain. Little anatomical detail can be gleaned from the heart – it lies in the
576 midline of the chest, with its apex resting near the median lobe of the liver. From surface
577 renderings, the two atria and single ventricle can be identified. Excellent descriptions of the
578 circulatory system of frogs (Ecker, 1889) and of *X. laevis* specifically (Grobbelaar, 1924) are
579 available in the literature.

580

581 **Discussion and Conclusions**

582 In this paper, we characterize the musculoskeletal, nervous, respiratory, digestive, and
583 urogenital anatomy of the key model organism *Xenopus laevis* for the first time in nearly a
584 century. We highlight the many unusual and unique morphological features of *X. laevis* (and
585 pipids) compared to other frogs, and attempt to resolve discrepancies in the identification
586 and nomenclature of various anatomical structures present in earlier publications. This was
587 accomplished by utilizing the emerging technique of diceCT to visualize the three-
588 dimensionally complex anatomy of *X. laevis*, the first such application of this method to
589 produce a full-body digital dissection of any anuran. This technique was particularly suitable in
590 this instance due to the small size of the specimen and delicate nature of the anatomical
591 structures. Furthermore, the method is non-destructive and replicable – our interpretation of
592 the anatomy of *X. laevis* can be checked by other researchers through examination of
593 original scan data. Lastly, this digital dissection preserves the 3D topological relationships of
594 the anatomical structures and more comprehensively illustrates the anatomy of *X. laevis*
595 than is possible in two-dimensional media.

596 Application of diceCT to other anurans (and vertebrate clades) will permit
597 researchers to bridge the gap between musculoskeletal anatomy and performance across
598 macroevolutionary time scales. Following the pioneering work of Emerson (1979), Reilly and
599 Jorgensen (2011) presented a new pattern for the evolution of pelvic bone morphology and
600 locomotor mode in Anura. However, some skeletal features (e.g., iliac ridges) occurred
601 across multiple locomotor modes while some locomotor styles (e.g., arboreal jumpers) could
602 not be diagnosed through skeletal characters. They suggested that other aspects of pelvic
603 design and function – notably differences in pelvic and hind limb myology – needed to be
604 compared across Anura to fully understand the evolution of locomotion in this clade. Our
605 study takes a first step towards this – for example, our digital dissection demonstrates that
606 the laterally-directed iliac ridges of *X. laevis* serve as attachment sites for (from anterior to
607 posterior): *M. latissimus dorsi*, the ligamentous plate, and the superficial and middle layers of
608 *M. iliacus externus*. The unique, short T-shaped urostyletic ridge serves as the attachment site
609 for *M. longissimus dorsi*. Coupled with information on pelvic and hind limb kinematics and
610 muscle activity during locomotion, we can now more fully understand the functional role of
611 these osteological characters in living and fossil frogs. Furthermore, the ability to visualize
612 nearly all soft tissues *in situ*, simultaneously and non-destructively makes it more likely that

613 very delicate structures will not be overlooked (such as the two muscles we visualized but
614 were unable to identify based on existing descriptions, see Results).

615 Our methods produced excellent resolution of the muscular anatomy – including
616 identification of over 110 different muscles within our specimen – and particularly clear
617 visualization of the nervous system. These results are presented in preceding illustrations as
618 well as fully interactive 3D PDFs included as supplementary information. Some limitations to
619 this study should be noted, including insufficient scan resolution to distinguish between the
620 very smallest muscles of the foot and hand (see Results for details). Additionally, although
621 our staining and scanning methods produced some visualization of the heart and of large,
622 proximal circulatory vessels, it could not resolve the majority of the circulatory system.
623 Alternative contrast-enhancing agents (such as BriteVu™) could be used to visualize arterial
624 and vascular trees in 3D (Gignac et al. 2016). Furthermore, our methods did not permit
625 visualization of muscle tendons (except those occurring inside muscles); using alternative
626 contrast agents known to bind to collagen fibres could help visualize tendinous structures
627 (Descamps et al., 2014) Lastly, this study details the anatomy of a young, post-metamorphic
628 individual, and it is known that the morphology of *X. laevis* changes during growth; future
629 anatomical studies of mature adults will permit detailed ontogenetic comparisons.

630 As showcased in this and other recent studies, diceCT provides a powerful new tool
631 for anatomical research, able to produce detailed, anatomical atlases of key or rare living
632 species for descriptive and educational purposes as well as 3D data suitable for further
633 morphometric, biomechanical and taxonomic studies.

634

635 **Data Accessibility**

636 The primary dataset for this article are the 3D PDFs, which have been uploaded as part of
637 the supplementary material; the reconstructions are available in other 3D formats upon
638 request to the corresponding author.

639

640 **Acknowledgements**

641 We thank additional members of our team Amber J. Collings and Enrico Eberhard (Royal
642 Veterinary College) as well as colleagues in the Structure and Motion Laboratory, particularly
643 Emily Sparkes and Timothy West, for their support. Animal care and husbandry was
644 provided by staff at the Biological Support Unit (RVC), with special thanks to Alastair Wallis.
645 Advice on I₂KI staining was shared by Jen Bright (University of South Florida), Philip Cox
646 (University of York), Paul Gignac (Oklahoma State University), Stephan Lautenschlager
647 (University of Bristol) and Maedeh Borhani (Imperial College London). Robert Asher and
648 Colin Shaw (University of Cambridge) provided access to CT-scanning facilities. Technical
649 support for Avizo was provided by Alejandra Sánchez-Eróstegui and Jean Luc-Garnier (FEI
650 Visualization Sciences Group). We have no competing interests.

651

652 **Author contributions**

653 LBP and RTC conceived of and designed the study; LBP carried out CT-scanning,
654 reconstructed, segmented and interpreted the CT data, and created the 3D PDFs; LBP
655 drafted the manuscript. Both authors gave final approval for publication.

656

657 **Funding**

658 This work was funded by an European Research Council (ERC) start grant (“PIPA : Paleo-
659 robotics and the innovations of propulsion in amphibians”) to RTC.

660

661 **References**

662
663 Ahn AN, Furrow E, Biewener AA (2004) Walking and running in the red-legged running frog
664 *Kassina maculata*. *J Exp Biol* **207**, 399-410.
665
666 Brocklehurst R, Porro LB, Herrel A, Adriaens D, Rayfield EJ (In prep) A digital dissection of
667 two teleost fishes: anatomy of soft- and hard-tissues in the heads of pike (*Esox lucius*) and
668 eel (*Anguilla anguilla*).
669
670 Burgess S (2016) A matched set of frog sequences. *Nature* **538**, 320-321.
671
672 Burggren WW, Warburton S (2007) Amphibians as animal models for laboratory research in
673 physiology. *ILAR J* **48**, 260-269.
674
675 Cannatella DC, Trueb L (1988) Evolution of pipoid frogs: intergeneric relationships of the
676 aquatic frog family Pipidae (Anura). *Zool J Linn Soc* **94**, 1-38.
677
678 Cannatella DC, de Sá RO (1993) *Xenopus* as a model organism. *Syst Biol* **42**, 476-507.
679
680 Clemente CJ, Richards CT (2013) Muscle dynamics and hydrodynamics limit power and
681 speed in swimming frogs. *Nature Comm* **4**, 2737.
682
683 Cline HT, Kelly BD (2012) *Xenopus* as an experimental system for development
684 neuroscience: Introduction to a special issue. *Develop Neurobiol* **72**, 463-464.
685
686 Cox, PG, Faulkes CG (2014) Digital dissection of the masticatory muscles of the naked
687 mole-rat, *Heterocephalus glaber* (Mammalia, Rodentia). *PeerJ* **2**, e448.
688
689 Cox PG, Jeffery N (2011) Reviewing the morphology of the jaw-closing musculature in
690 squirrels, rats, and guinea pigs with contrast-enhanced micro-CT. *Anat Rec* **294**, 915-928.
691
692 Descamps E, Sochacka A, DeKegel B, Van Loo D, Van Hoorebeke L, Adriaens D. (2014)
693 Soft tissue discrimination with contrast agents using micro-CT scanning. *Belg J Zool* **144**,
694 20-40.
695
696 Diogo R, Ziermann JM. (2009) Development of fore- and hindlimb muscles in frogs:
697 morphogenesis, homeotic transformations, digit reduction, and the forelimb-hindlimb enigma.
698 *J Exp Zool B Mol Dev Evol* **322B**, 86-105.
699
700 Dunlap DG (1960) The comparative myology of the pelvic appendage in the Salientia. *J*
701 *Morphol* **106**, 1-76.
702
703 Düring DN, Ziegler A, Thomason CK et al. (2013) The songbird syrinx morpheme: a three-
704 dimensional, high-resolution, interactive morphological map of the zebra finch vocal organ.
705 *BMC Biol* **11**, 1.
706
707 Ecker A (1889) *The Anatomy of the Frog*. Oxford: Clarendon Press.
708
709 Emerson SB (1979) The ilio-sacral articulation in frogs: form and function. *Biol J Linn Soc*
710 **11**, 153-168.
711

712 Emerson SB (1982) Frog postcranial morphology: identification of a functional complex.
713 *Copeia* **3**, 603-613.
714

715 Evans BJ, Carter TF, Greenbaum E et al. (2015) Genetics, morphology, advertisement calls,
716 and historical records distinguish six new polyploid species of African clawed frog (*Xenopus*,
717 Pipidae) from West and Central Africa. *PLOS ONE* **10**, e0142823.
718

719 Gignac PM, Kley NJ, Clarke JA et al. (2016) Diffusible iodine-based contrast-enhanced
720 computed tomography (diceCT): an emerging tool for rapid, high-resolution, 3D imaging of
721 metazoan soft tissues. *J Anat* doi:10.1111/joa.12449.
722

723 Green TL (1931) On the pelvis of Anura: a study in adaptation and recapitulation. *Proc Zool*
724 *Soc Lond* **101**, 1259-1290.
725

726 Grobbelaar CS (1924) Beiträge zu einer anatomischen Monographie von *Xenopus laevis*
727 (Daud.). *Z Anat Entwicklungs* **72**, 131-168.
728

729 Gross JB, Hanken J (2008) Segmentation of the vertebrate skull: neural-crest derivation of
730 adult cartilages in the clawed frog, *Xenopus laevis*. *Integ Comp Biol* **48**, 681-696.
731

732 Gurdon JB, Hopwood N (2000) The introduction of *Xenopus laevis* into developmental
733 biology: of empire, pregnancy testing and ribosomal genes. *Int J Dev Biol* **44**, 43-50.
734

735 Gurdon JB, Elsdale TR, Fischberg M (1958) Sexually mature individuals of *Xenopus laevis*
736 from the transplantation of single somatic nuclei. *Nature* **182**, 64-65.
737

738 Gurdon JB, Lane CD, Woodland HR, Marbaix B (1971) Use of frog eggs and oocytes for the
739 study of messenger RNA and its translation in living cells. *Nature* **233**, 177-182.
740

741 Harland RM, Grainger RM (2011) *Xenopus* research: metamorphosed by genetics and
742 genomics. *Trends Genet* **27**, 507-515.
743

744 Hass A (2001) Mandibular arm musculature of anuran tadpoles, with comments on
745 homologies of amphibian jaw muscles. *J Morphol* **247**, 1-33.
746

747 Hautier L, Lebrun R, Cox PG (2012) Patterns of covariation in the masticatory apparatus of
748 hystricognath rodents: implications for evolution and diversification. *J Morphol* **273**, 1319-
749 1337.
750

751 Hellsten U, Harland RM, Gilchrist MJ et al. (2010) The genome of the western clawed frog
752 *Xenopus tropicalis*. *Science* **328**, 633-636.
753

754 Holliday CM, Tsai HP, Skiljan RJ, et al. (2013) A 3-D interactive model and atlas of the jaw
755 musculature of *Alligator mississippiensis*, *PLOS ONE* **8**, e62806.
756

757 Jeffery NS, Stephenson RS, Gallagher JA et al. (2011) Microcomputed tomography with
758 iodine staining resolves the arrangement of muscle fibres. *J Biomech* **44**, 189-192.
759

760 Johnston P. (2011) Cranial muscles of the anurans *Leiopelma hochstetteri* and *Ascaphus*
761 *truei* and the homologies of the mandibular adductors in Lissamphibia and other
762 gnathostomes. *J Morphol* **272**: 1492-1512.

763
764 Kargo WJ, Nelson F, Rome L. (2002) Jumping in frogs: assessing the design of the skeletal
765 system by anatomically realistic modeling and forward dynamic simulation. *J Exp Biol* **205**,
766 1683-1702.
767
768 Kleinteich T, Conway KW, Gorb SN et al. (2014) What's inside a fish suction cup? *Bruker*
769 *microCT User Mtg Abstracts* **2014**, 1-4.
770
771 Kleinteich T, Gorb SN (2015a) The diversity of sticky frog tongues. *Bruker microCT User Mtg*
772 *Abstracts* **2015**, 1-4.
773
774 Kleinteich T, Gorb SN (2015b) Frog tongue acts as muscle-powered adhesive tape. *R Soc*
775 *Open Sci* **2**, 150333.
776
777 Lautenschlager S, Bright JA, Rayfield EJ (2013) Digital dissection – using contrast-enhanced
778 computed tomography scanning to elucidate hard- and soft-tissue anatomy of the Common
779 Buzzard *Buteo buteo*. *J Anat* **224**, 412-431.
780
781 Lautenschlager S, Ruecklin M (2014) Beyond the print – virtual paleontology in science
782 publishing, outreach, and education. *J Paleont* **88**, 727-734.
783
784 Mason MJ, Wang M, Narins PM (2009) Structure and function of the middle ear apparatus of
785 the aquatic frog, *Xenopus laevis*. *Proc Inst Acoust* **31**, 13-21.
786
787 Metscher BD (2009a) Micro-CT for comparative morphology: simple staining methods allow
788 high-contrast 3D imaging of diverse non-mineralized animal tissues. *BMC Physiol* **9**, 11.
789
790 Metscher BD (2009b) Micro-CT for developmental biology: a versatile too for high-contrast 3-
791 D imaging. *Dev Dyn* **238**, 632-640.
792
793 Metscher BD (2013) Biological applications of X-ray microtomography: imaging micro-
794 anatomy, molecular expression and rganismal diversity. *Micrsosc Anal* **27**, 13-16.
795
796 Minkoff EC (1975) *A Laboratory Guide to Frog Anatomy*. New York: Pergamon Press.
797
798 Palmer M (1960) Expanded ilio-sacral joint in the toad *Xenopus laevis*. *Nature* **187**, 797-798.
799
800 Paterson NF (1939) The head of *Xenopus laevis*. *Quart J Microscop Sci* **81**, 161-234.
801
802 Přikryl T, Aerts P, Havelková P et al. (2009) Pelvic and thigh musculature in frogs (Anura)
803 and origin of anuran jumping locomotion. *J Anat* **214**, 100-139.
804
805 Pyron AR, Wiens JI (2011) A large-scale phylogeny of the Amphibia including over 2800
806 species, and a revised classification of extant frogs, salamanders, and caecilians. *Mol*
807 *Phylogenet Evol* **61**, 543-583.
808
809 Porro LB, Collings AC, Eberhard E, Chadwick K, Richards CT (Accepted) Inverse dynamic
810 modelling of jumping in the red-legged running frog *Kassina maculata*. *J Exp Biol*.
811

812 Quayle MR, Barnes DG, Kaluza OL, McHenry CR. 2014. An interactive three-dimensional
813 approach to anatomical description – the jaw musculature of the Australian laughing
814 kookaburra (*Dacelo novaeguineae*). *PeerJ* **2**, e355.
815

816 Reilly S, Jorgensen M (2011). The evolution of jumping in frogs: morphological evidence for
817 the basal anuran locomotor condition and the radiation of locomotor systems in crown group
818 anurans. *J. Morph.* **272**, 149-168.

819 Richards CT, Clemente CJ (2013) Built for rowing: frog muscle is tuned to limb morphology
820 to power swimming. *J Roy Soc Inter* **10**, 20130236.
821

822 Robovská-Havelková P (2010) How can ontogeny help us understand the morphology of the
823 anuran pectoral girdle? *Zoomorphol* **129**, 121-132.
824

825 Robovská-Havelková P, Aerts P, Roček Z, Prikryl T, Fabre A-C, Herrel A (2014) Do all frogs
826 swim alike? The effect of ecological specilization on swimming kinematics in frogs. *J Exp*
827 *Biol* **217**, 3637-3644.
828

829 Roček Z (1993) Origin and evolution of the anuran postnasal wall and adjacent parts of
830 palatoquadrate. *Ethol Ecol Evol* **5**, 247-265.
831

832 Ročkova H, Roček Z (2005) Development of the pelvis and posterior part of the vertebral
833 column in the Anura. *J Anat* **206**, 17-35.
834

835 Ryke PAJ (1953) The ontogenetic development of the somatic musculature of the trunk of
836 the aglossal anuran *Xenopus laevis* (Daudin). *Acta Zool* **34**, 1-70.
837

838 Sassoon D, Kelley DB (1986) The sexually dimorphic larynx of *Xenopus laevis*: development
839 and androgen regulation. *Am J Anat* **177**, 457-472.
840

841 Session AM, Uno Y, Kwon T, et al. (2016) Genome evolution in the allotetraploid frog
842 *Xenopus laevis*. *Nature* **538**, 336-343.
843

844 Smirnov SV (1994) Postmaturation skull development in *Xenopus laevis* (Anura, Pipidae):
845 late-appearing bones and their bearing on the pipid ancestral morphology. *Russian J*
846 *Herpetol* **1**, 21-29.
847

848 Trueb L, Hanken J (1992) Skeletal development in *Xenopus laevis* (Anura: Pipidae). *J*
849 *Morphol* **214**, 1-41.
850

851 Tsai HP, Holliday CM (2011) Ontogeny of the alligator cartilage transiliens and its
852 significance for sauropsid jaw muscle evolution. *PLOS ONE* **6**, e24935.
853

854 Van Dijk DE (2002) Longitudinal sliding articulations in pipid frogs. *S Afr J Sci* **98**, 555-556.
855

856 Wheeler GN, Brändli AW (2009) Simple vertebrate models for chemical genetics and drug
857 discovery screens: lessons from zebrafish and *Xenopus*. *Dev Dyn* **238**, 1287-1308.
858

859 Whiting HP (1961) Pelvic girdle in amphibian locomotion. *Symp Zool Soc Lond* **5**, 43-57.
860

861 Ziermann JM, Olsson L (2007) Patterns of spatial and temporal cranial muscle development
862 in the African Clawed Frog, *Xenopus laevis* (Anura: Pipidae). *J Morphol* **268**, 791-804.

863

864 Ziermann JM, Diogo R (2014) Cranial muscle development in frogs with different
865 developmental modes: direct development versus biphasic development. *J Morphol* **275**,
866 398-413.

867

868 **Supplementary Material**

869

870 **Fig. S1.** Interactive 3D PDF of the digitally segmented skeleton of *Xenopus laevis*. Click on
871 the reconstruction to activate. Left click and drag to rotate, right click and drag to zoom in
872 and out, click both buttons and drag to pan. Open model tree on the upper toolbar to show or
873 hide individual parts.

874

875 **Fig. S2.** Interactive 3D PDF of the digitally segmented musculature of *Xenopus laevis*; with
876 the exception of *m. longissimus dorsi*, only right side muscles are shown.

877

878 **Fig. S3.** Interactive 3D PDF of the digitally segmented nervous system of *Xenopus laevis*.

879

880 **Fig. S4.** Interactive 3D PDF of the digitally segmented digestive, urogenital and respiratory
881 systems of *Xenopus laevis*.

882

883

884

885

886

887

888

889

Tables

Table 1. Origin and insertion sites for muscles in *Xenopus laevis*.

Muscle	Abbreviation	Origin	Insertion
<u>Head and throat muscles</u>			
<i>M. rectus superior</i>	RCS	Prootic, tendon from parasphenoid	Posterodorsal surface of eyeball
<i>M. rectus inferior</i>	RCI	Tendon from parasphenoid	Ventral surface of eyeball
<i>M. rectus anterior (medialis)</i>	RCA	Tendon from parasphenoid	Medial surface of eyeball
<i>M. rectus posterior (lateralis)</i>	RCP	Tendon from parasphenoid	Posteroventral surface of eyeball
<i>M. obliquus superior</i>	OBS	Parasphenoid	Dorsomedial surface of eyeball
<i>M. obliquus inferior</i>	OBI	Parasphenoid	Anteroventral surface of eyeball
<i>M. retractor bulbi</i>	RB', RB'', RB'''	Parasphenoid	Posteroventral and posteromedial surface of eyeball
<i>M. levator bulbi</i>	LB	Frontoparietal, sphenethmoid	Pterygoid
<i>M. adductor mandibulae A2 and A2 lateralis</i>	A2	Anteroventral margin of the squamosal	Lateral aspect of the angulosplenic
<i>M. adductor mandibulae A2 posteroventromesial + A3'</i>	A3'	Lateral aspect of prootic-exoccipital, posterolateral margin of frontoparietal, dorsomedial aspect of anterior process of squamosal	Lateral aspect of coronoid process of the angulosplenic
<i>M. adductor mandibulae A3''</i>	A3''	Anterolateral aspect of prootic-exoccipital, lateral margin of frontoparietal	Dorsal margin of coronoid process of angulosplenic
<i>M. depressor mandibulae</i>	DM	Dorsal fascia and lateral aspect of prootic-exoccipital dorsal to stapes (outer part); posteroventral corner of squamosal and tympanic ring (inner part)	Posterodorsal tip of angulosplenic
<i>M. intermandibularis anterior</i>	IMA	Medial surface of anterior dentary	Same as origin
<i>M. intermandibularis posterior</i>	IMP	Dorsomedial surfaces of dentary, pterygoid/prootic	Midline raphe
<i>M. geniohyoideus</i>	GHY	Medial surface of anteriormost dentary	Hyoid bone and cartilage
<i>M. sternohyoideus</i>	SHY	Continuation of <i>M. rectus abdominus</i>	Hyoid bone and cartilage
<i>M. petrohyoideus (posterior)</i>	PHY	Prootic-exoccipital	Hyoid bone and cartilage
<i>M. dilator laryngis</i>	LAR	Cartilages of the larynx	Same as origin
<u>Back and abdominal muscles</u>			

<i>M. longissimus dorsi</i>	LGD	Spinous and transverse vertebral processes, occiput	Dorsal aspect of anterior half of urostyle
<i>M. coccygeoiliacus</i>	CGI	Lateral aspect of the urostyle	Medial surface of anterior third of ilium
<i>M. iliolumbaris</i>	IL	Lateroventral aspect of vertebrae 1 - 4, tip of transverse process of 4th vertebra	Lateroventral aspect of anterior tip of ilium
<i>M. intertransversarii</i>	ITR	Between adjacent transverse processes	Same as origin
<i>M. intertransversarius capitis superior</i>	ICS	Posterior aspect of prootic	Distal tip of transverse process of 2nd vertebra
<i>M. intertransversarius capitis inferior</i>	ICI	Posteroventral aspect of prootic	Distal tip of transverse process of 2nd vertebra
<i>M. obliquus externus</i>	OBE	Dorsal fascia, ligamentous plate	Ventral aponeurosis, linea alba
<i>M. transversus abdominis</i>	TRA	Dorsal fascia, ligamentous plate	Ventral aponeurosis, linea alba; sternum and pharynx
<i>M. rectus abdominus superficialis</i>	RAS	<i>M. rectus abdominis profundus</i> , linea alba	<i>M. pectoralis</i> , scapula
<u>Pectoral and forelimb muscles</u>			
<i>M. cucullaris</i>	CUL	Stapes, otic capsule and tympanic annulus	Medial aspect of anterior margin of scapula
<i>M. rhomboideus anterior</i>	RBA	Posterodorsal aspect of exoccipital	Anterodorsal tip of suprascapula
<i>M. levator scapulae superior</i>	LSS	Lateral aspect of prootic-exoccipital	Medial aspect of posterodorsal suprascapula
<i>M. levator scapulae inferior</i>	LSI	Ventral aspect of prootic-exoccipital and parasphenoid	Medial aspect of posteroventral suprascapula
<i>M. latissimus dorsi</i>	LTD	Dorsal fascia	Dorsal surface of deltoid crest (tuberosity) of humerus
<i>M. serratus superior</i>	SRS	Dorsal fascia, distal tips of third and fourth vertebral processes	Dorsal margin of suprascapula
<i>M. serratus medius</i>	SRM	Distal tip of third transverse vertebral process	Medial aspect of suprascapula
<i>M. serratus inferior</i>	SRI	Distal tips of third and fourth transverse vertebral processes	Medial aspect of ventral suprascapula/dorsal scapula

<i>M. pectoralis (pars abdominalis)</i>	PEC	Ventral fascia, linea alba, <i>M. rectus abdominus</i>	Ventral surface of deltoid crest of humerus
<i>M. pectoralis (pars anterior sternalis)</i>	PEC'	Ventral aspect of coracoid, sternal bones/cartilages	Ventral surface of deltoid crest of humerus
<i>M. pectoralis (pars posterior sternalis)</i>	PEC''	Posterior aspect of coracoid, sternal bones/cartilages	Ventral surface of deltoid crest of humerus
<i>M. sternoradialis</i>	STR	Sternal bones/cartilages, clavicle	Ventral/medial aspect of proximal radioulna
<i>M. coracobrachialis</i>	CRH	Coracoid and sternum	Humerus, adjacent to the deltoid crest
<i>M. deltoideus</i>	DEL	Lateral (external) aspect of scapula, lateral margin of clavicle, sternal bones/cartilages	Lateral aspect of distal humerus
<i>M. interscapularis</i>	ISC	Medial (internal) aspect of suprascapula	Medial (internal) aspect of scapula
<i>M. subscapularis</i>	SSC	Posterior margin of medial (internal) aspect of scapula	Ventral aspect of humerus
<i>M. scapulo-humeralis profundus posterior</i>	SHP	Posterior to glenoid of scapula	Dorsal aspect of proximal humerus
<i>M. dorsalis scapulae</i>	DSC	Lateral (external) aspect of ventral suprascapula	Dorsal surface of deltoid crest of humerus
Unknown pectoral girdle muscle	u	Dorsal aspect of distal tip of coracoid	Anteromedial aspect of scapula
<i>M. triceps brachii (long head)</i>	TRI	Posterior margin of scapula adjacent to glenoid	Tendon to proximal end of radioulna
<i>M. triceps brachii (outer [lateral] head)</i>	TRI'	Dorsal and lateral aspects of humerus	Tendon to proximal end of radioulna
<i>M. triceps brachii (inner [medial] head)</i>	TRI''	Ventral and medial aspects of humerus	Tendon to proximal end of radioulna
<i>M. flexor carpi radialis</i>	FCR	Medial aspect of distal humerus	Carpal bones
<i>M. flexor carpi ulnaris</i>	FCU	Medial aspect of distal humerus	Carpal bones
<i>M. flexor digitorum communis</i>	FDC	Medial aspect of distal humerus	Palmar aponeurosis of hand
<i>M. flexor antebrachii medius</i>	FAM	Medial aspect of distal humerus	Ventral surface of middle radioulna
<i>M. flexor antebrachii lateralis superficialis</i>	FALS	Medial epicondyle of humerus	Carpal bones and radioulna

<i>M. flexor antebrachii lateralis profundus</i>	FALP	Medial epicondyle of humerus	Radioulna
<u>Pelvic and hind limb muscles</u>			
<i>M. iliacus externus</i> outer layer	IE	Ventral aspect of ligamentous plate, dorsolateral aspect of middle iliac shaft	Anterodorsal aspect of proximal femur
<i>M. iliacus externus</i> middle layer	IE'	Lateral, dorsal and medial aspects of iliac shaft	Anterodorsal aspect of proximal femur, proximal to insertion of IE
<i>M. iliacus externus</i> middle layer (extra portion)	IE''	Ventral aspect of ligamentous plate, medial aspect of posterior iliac shaft	Same as <i>M. iliacus externus</i> middle layer
<i>M. iliacus externus</i> deep layer	IE'''	Lateral, ventral and medial aspects of iliac shaft	Dorsal aspect of proximal femur, between insertions of outer and extra middle layers of <i>M. iliacus externus</i>
<i>M. iliacus internus</i>	II	Lateral, ventral and medial aspects of posterior iliac shaft	Anterodorsal aspect of femur, distal to IE insertions
<i>M. pyriformis</i>	PY	Dorsolateral aspect of mid urostyle	Dorsal aspect of femoral head
<i>M. tensor fascia latae</i>	TFL	Fascia covering ventral aspect of deep layer of <i>M. iliacus externus</i>	Fascia covering anterior aspect of <i>M. cruralis</i>
<i>M. cruralis</i>	CR	Ventrolateral aspect of ilium anteroventral to acetabulum	Knee aponeurosis
<i>M. gluteus magnus</i>	GLM	Lateral aspect of dorsal process of ilium, anterior and dorsal to the origin of <i>M. iliofibularis</i>	Knee aponeurosis, fascia of <i>M. cruralis</i>
<i>M. iliofemoralis</i>	IFM	Lateral aspect of dorsal process of ilium, posterior and ventral to origin of <i>M. iliofibularis</i>	Along dorsal aspect of proximal half of femur
<i>M. gracilis major</i>	GMA	Lateral aspect of posteroventral ischial rim	Posterior aspect of medial tibiofibular head, distal to insertion of <i>M. semitendinosus</i>
<i>M. gracilis minor</i>	GMI	Posterolateral tip of ischium, wall of cloaca	Combined insertion with <i>M. gracilis major</i>
<i>M. semimembranosus</i>	SM	Lateral aspect of posterodorsal ischial rim	Posterior aspect of medial tibiofibular head

<i>M. semitendinosus</i>	ST	Lateral aspect of ventral ischial rim	Posterior aspect of medial tibiofibular head, distal to insertion of <i>M. semimembranosus</i>
<i>M. sartorius</i>	SA	Praepubis	Knee aponeurosis and medial aspect of tibiofibular head
<i>M. adductor magnus</i> dorsal head	ADD	Lateral aspect of ischial rim, anterior to origin of <i>M. gracilis major</i>	Posterior aspect of proximal half of femur; dorsal and anterior aspects of distal half of femur
<i>M. adductor magnus</i> ventral head	ADV	Lateral aspect of ischial rim, anterior to origin of dorsal head of <i>M. adductor magnus</i>	Ventral aspect of femur
<i>M. pectineus</i> (and <i>M. adductor longus</i>)	PT-ADL	Lateral aspects of the anteroventral ilium and anterior pubis	Ventral aspect of proximal femur
<i>M. obturator externus</i> (and <i>M. quadratus femoris</i>)	OBE-QF	Lateral aspect of dorsal ischium, surrounding acetabulum	Dorsal aspect of femoral head
<i>M. obturator internus</i>	OBI	Lateral aspect of ventral ischium, surrounding acetabulum	Ventral aspect of femoral head
<i>M. gemellus</i>	GML	Lateral aspect of posterodorsal ischial rim, between origins of <i>M. semimembranosus</i> and <i>M. obturator externus</i>	Posterodorsal aspect of proximal femur
<i>M. iliofibularis</i>	IFB	Lateral aspect of dorsal process of ilium, between origins of <i>M. gluteus magnus</i> and <i>M. iliofemoralis</i>	Posterodorsal aspect of lateral tibiofibular head via tendon
<i>M. plantaris longus</i>	PL	Knee aponeurosis, posterodorsal aspect of distal femur, posterolateral aspect of proximal tibiofibula	Plantaris tendon
<i>M. peroneus</i>	PE	Knee aponeurosis, anterolateral aspect of proximal tibiofibula	Anterolateral aspect of distal tibiofibula, lateral aspect of proximal head of the calcaneum
<i>M. tibialis posticus</i>	TBP	Posterior aspect of distal half of tibiofibula	Tendon to the astragalus
<i>M. tibialis anticus longus</i>	TAL	Dorsal aspect of lateral femoral condyle	Anterolateral aspect of proximal head of the calcaneum, anteromedial aspect of proximal head of the astragalus
<i>M. tibialis anticus brevis</i>	TAB	Anteromedial aspect of the tibiofibula	Medial aspect of head of the astragalus

<i>M. extensor cruris brevis</i>	ECB	Knee aponeurosis	Anterior aspect of proximal tibiofibula
<i>M. tarsalis anticus</i>	TA	Anterolateral distal tibiofibula	Anterolateral aspect of astragalus
<i>M. tarsalis posticus/M. plantar profundus</i>	TP/PP	Medial border of plantaris tendon	Posterior aspect of astragalus, tendon to prehallux
<i>M. flexor digitorum brevis superficialis</i>	FDBS	Lateral border of plantaris tendon	Superficial flexor tendons to digits II - V
<i>M. intertarsalis</i>	IT	Lateral aspect of calcaneum and medial aspect of astragalus	Distal tarsal bones
<i>M. extensor digitorum communis longus</i>	EDCL	Lateral margin of <i>M. tarsalis anticus</i>	<i>M. extensores breves</i>
<i>M. abductor brevis dorsalis digiti V</i>	ABD 5	Anterior aspect of calcaneum	Lateral aspect of proximal metatarsal V
<i>M. abductor brevis plantaris hallucis</i>	ABPH	Lateral aspect of <i>M. plantaris profundus</i> and prehallux	Ventral aspect of distal metatarsal I
<i>M. lumbricales breves digitorum II - V, M. lumbricales longus digitorum III - V and M. lumbricales longissimus digiti IV</i>	LUM 2-5	Plantar tendon, superficial flexor tendons	Ventral surface of corresponding metatarso-digital joint, base of second phalanges of digits III – V, base of third phalanx of digit IV
<i>M. interphalangeales digitorum III - V and M. interphalangealis distalis digiti IV</i>	IPD	Ventral surface of proximal phalanx, and second phalanx of digit IV	Ventral surface of second phalanx, and third phalanx of digit IV
<i>M. abductor brevis plantaris digiti V</i>	ABP 5	Posterolateral tip of calcaneum	Lateroventral aspect of metatarsal V
<i>M. extensor brevis superficialis hallucis</i>	EBS 1	Anteromedial aspect of the calcaneum	Dorsolateral surface of metatarsal I
<i>M. extensores breves superficiales digitorum II - IV</i>	EBS 2 - 4	Medial aspect of distal calcaneum	Proximal head of second phalanx
<i>M. extensor brevis medius digiti II</i>	EBM 2	Lateral aspect of distal astragalus	Same as <i>M. extensor brevis superficialis II</i>
<i>M. extensores breves profundii digitorum II - IV</i>	EBP 2 - 4	Lateral border of metatarsus	Long tendons to distal phalanx
<i>M. abductor brevis dorsalis hallucis</i>	ABDH	Medial aspect of distal astragalus	Dorsomedial aspect of metatarsal I
Unknown foot muscle	u	Ventral aspect of metatarsal I	Ventral aspect of metatarsal I

Figure Legends

Fig. 1 Coronal/transverse μ CT sections of *X. laevis* specimen before (A, C, E) and after staining with I_2KI (B, D, F). Position of sections through the head (A, B), abdomen (C, D) and pelvis/hind limb (E, F) are shown in G.

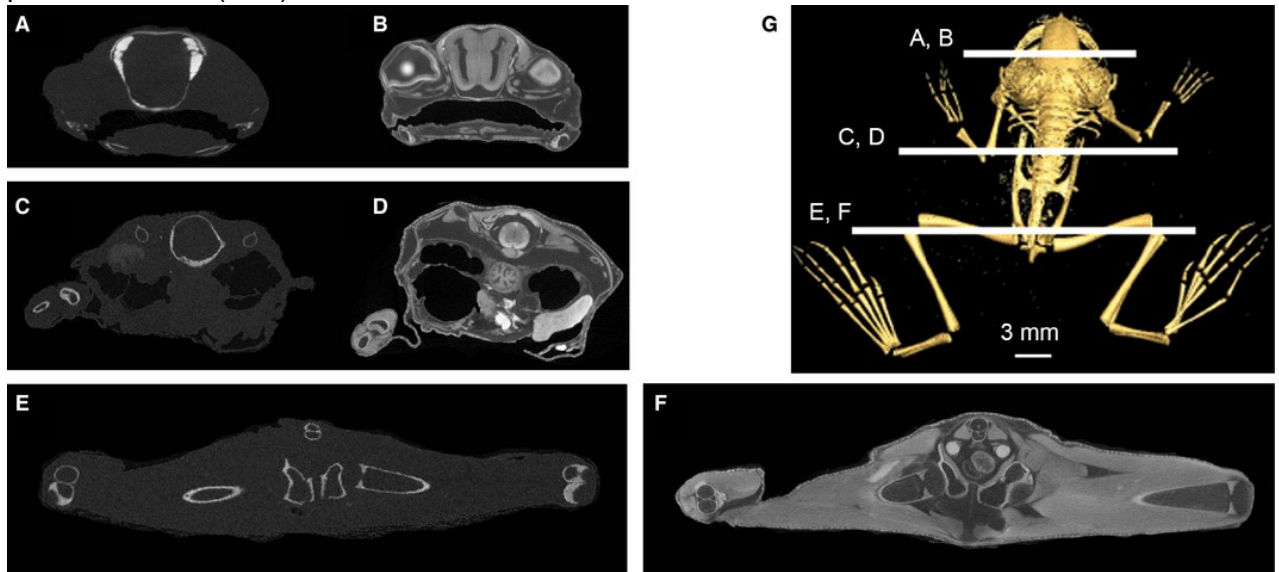


Fig. 2 Skull osteology of *Xenopus laevis* (A, C, E, G) and *Kassina maculata* (B, D, F, H). Crania (upper jaw) in dorsal (A, B) and ventral (C, D) views; skull and lower jaw in lateral view (E, F); lower jaw in dorsal view (G, H). Abbreviations: AN, angulosplenial; CM, columnella; D, dentary; MN, mentomeckelian; MX, maxilla; N, nasal; PL, palatine; PMX, premaxilla; PRO/EXO, prootic-exoccipital; PS, parasphenoid; PT, pterygoid; Q, quadrate; QJ, quadratojugal; SE, sphenethmoid; SP, septomaxilla; SQ, squamosal; V, vomer.

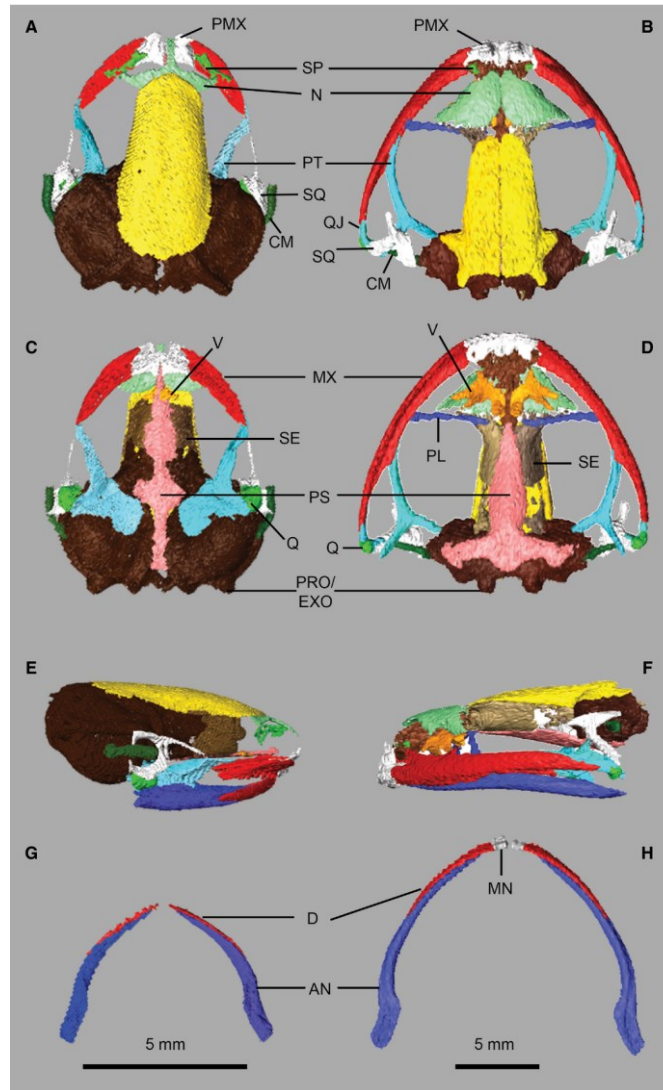


Fig. 3 Postcranial osteology of *Xenopus laevis* (A, C) and *Kassina maculata* (B, D) shown in dorsal (A, B) and ventral (C, D) views. Abbreviations: AS, astragalus; CA, calcaneum; CL, clavicle; CO, coracoid; F, femur; H, humerus; IC, ischium; IL, ilium; MC, metacarpals; ME, mesosternum; MT, metatarsals; OM, omosternum; PH, phalanges; PU, pubis; RU, radioulna; S, sacral vertebrae; SC, scapula; SS, suprascapula; SU, fused sacrourostyle; TF, tibiofibula; U, urostyle; V, vertebrae.

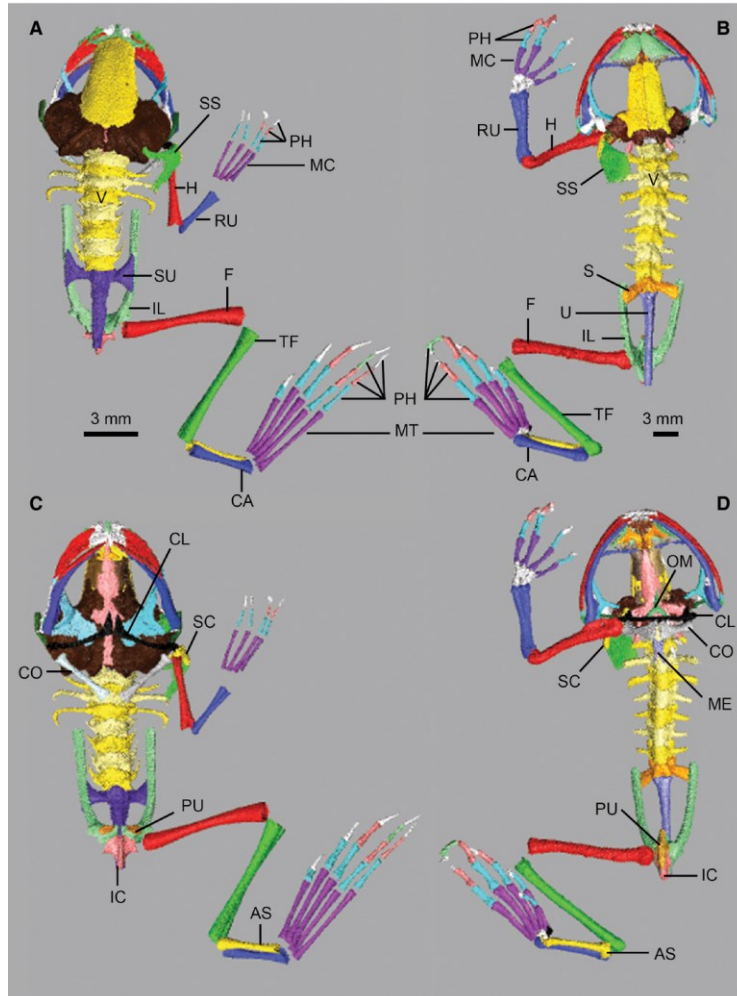


Fig. 4 Head musculature of *Xenopus laevis*. Musculature of the right orbit in posterolateral (A) and posteromedial (B) views, and in transverse cross-section through the base of the eyeball (C). Jaw musculature in anterolateral view (D) and transverse cross-section through the coronoid process (E), and jaw muscle attachments on the skull upper and lower jaws (F). Hyoid musculature in ventral view (G) and posterior oblique view (H) with the skull transparent. Main muscle masses are identified using uppercase abbreviations; muscle attachment sites, small muscle slips and non-muscle structures are identified using lowercase abbreviations. Abbreviations: A2, *M. adductor mandibulae A2* (masseter); a2, attachments of A2; A3', *M. adductor mandibular A2 PVM* and A3' (temporalis); a3', attachments of A3'; A3'', *M. adductor mandibulae A3''* (pterygoideus); a3'', attachments of A3''; CN II, optic nerve; ct, central tendon; CUL, *M. cucullaris*; DM, *M. depressor mandibulae*; dm, attachments of DM; GHY, *M. geniohyoideus*; IMA, *m M intermandibularis anterior*, IMP, *M. intermandibularis posterior*, LB, *M. levator bulbi*; PHY, *M. petrohyoideus posterior*, OBI, *M. obliquus inferior*, OBS, *M. obliquus superior*, RB'/RB''/RB'''', portions of *M. retractor bulbi*; RCA, *m M rectus anterior*, RCI, *M. rectus inferior*, RCP, *M. rectus posterior*, RCS, *M. rectus superior*, sd, subhyoideus portion of IMP; SHY, *M. sternohyoideus*.

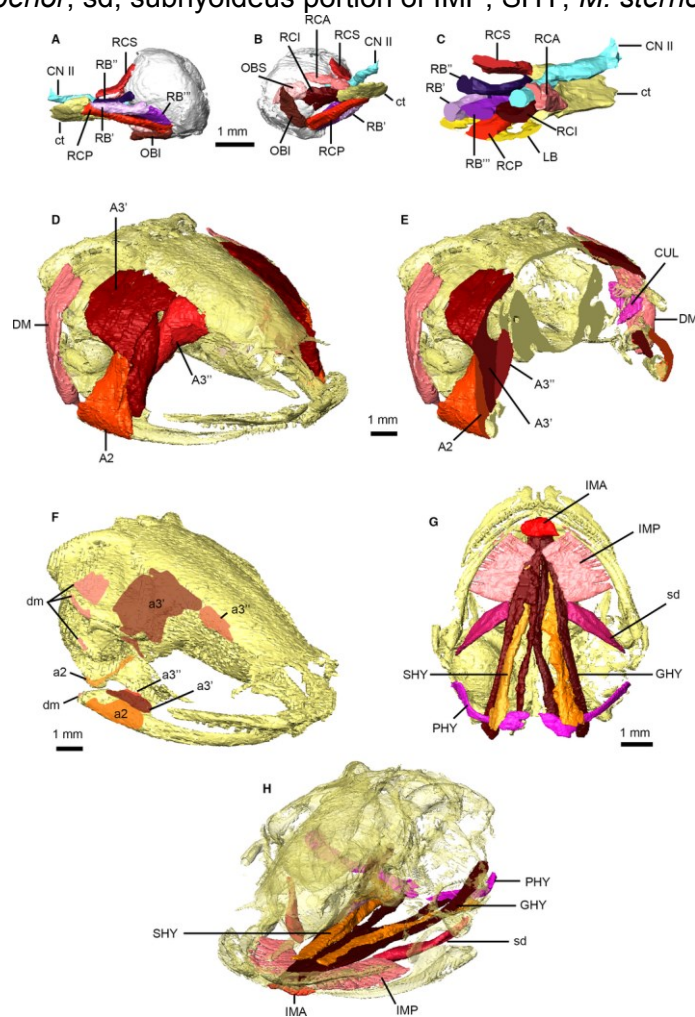


Fig. 5 Back and abdominal musculature of *Xenopus laevis*; both sides of *M. longissimus dorsi* and *M. coccygeiliacus* are shown, otherwise only right side structures are depicted. Specimen shown in oblique view (A); dorsal view with ligamentous plate, *M. longissimus dorsi* and *M. latissimus dorsi* removed (B); ventral view (C); and transverse cross-sections (D, E) shown in A. Muscles are identified using uppercase abbreviations; non-muscle structures are identified using lowercase abbreviations. Abbreviations: CGI, *M. coccygeiliacus*; ICI, *M. intertransversarius capitis inferior*; ICS, *M. intertransversarius capitis superior*; IL, *M. iliolumbaris*; ITR, *M. intertransversarii*; LGD, *M. longissimus dorsi*; lp, ligamentous plate; LTD, *M. latissimus dorsi*; OBE, *M. obliquus externus*; PEC, *M. pectoralis pars abdominalis*; RAP, *M. rectus abdominus profundus*; RAS, *M. abdominus superficialis*; TRA, *M. transversus abdominus*.

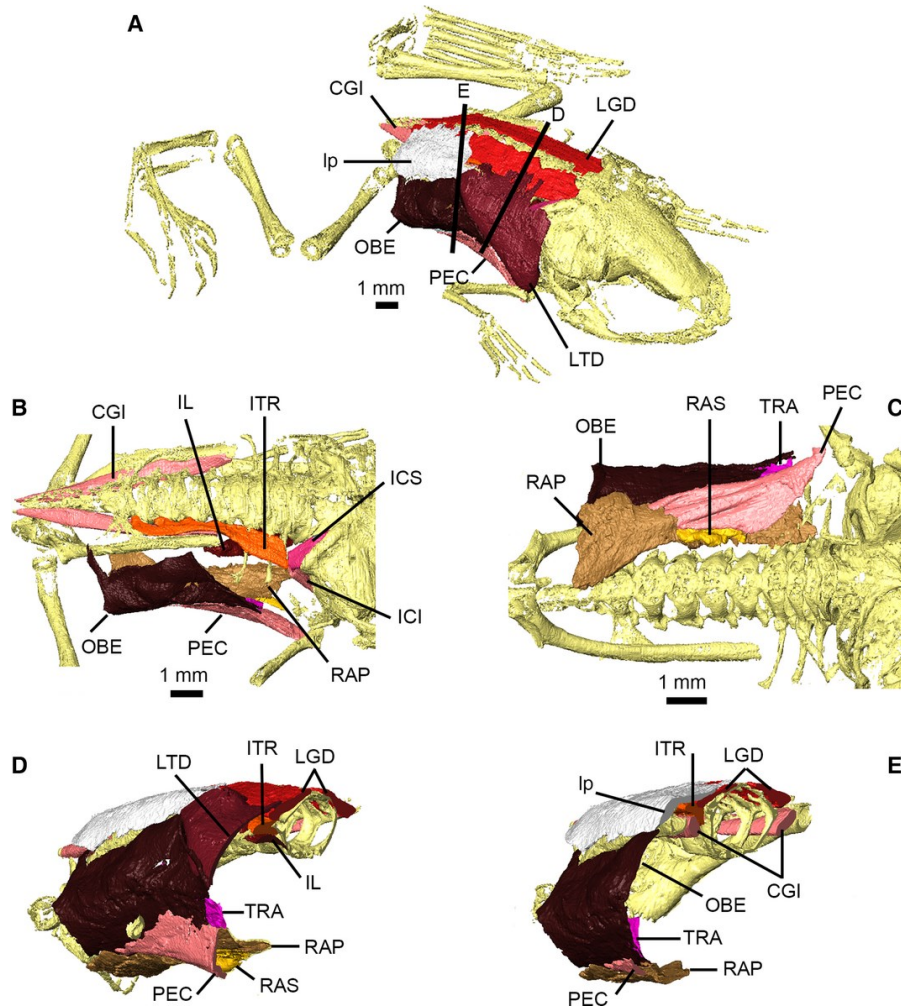


Fig. 6 Pectoral and forelimb musculature of *Xenopus laevis*. Dorsal pectoral musculature shown in right dorsolateral view (A) with *M. depressor mandibulae* and *M. latissimus dorsi* transparent, right posterolateral view (B) with right suprascapula transparent, and right dorsolateral view (C) with suprascapula transparent. Ventral pectoral and arm musculature shown in ventral (D) and posterior (E) views. Dorsal view of specimen (F) detailing locations of transverse cross-sections through pectoral musculature (G, H). Arm and forearm musculature in dorsal (I) and ventral (J) views, and transverse cross-sections through the arm (K) and forearm (L), with sections shown in I and J. Main muscles are identified using uppercase abbreviations; muscle slips and non-muscle structures are identified using lowercase abbreviations. Abbreviations: CRH, *M. coracohumeralis*; CUL, *M. cucullaris*; DEL, *M. deltoideus*; DM, *M. depressor mandibulae*; DSC, *M. dorsalis scapulae*; FAM, *M. flexor antebrachii medius*; FALP, *M. flexor antebrachii lateralis profundus*; FALS, *M. flexor antebrachii lateralis superficialis*; FCR, *M. flexor carpi radialis*; FCU, *M. flexor carpi ulnaris*; FDC, *M. flexor digitorum communis*; ICI, *M. intertransversarius capitis inferior*; ICS, *M. intertransversarius capitis superior*; ISC, *M. interscapularis*; LGD, *M. longissimus dorsi*; LSI, *M. levator scapulae inferior*; LSS, *M. levator scapulae superior*; LTD, *M. latissimus dorsi*; PEC, *M. pectoralis pars abdominalis*; PEC', *M. pectoralis pars anterior sternalis*; PEC'', *M. pectoralis pars posterior sternalis*; RBA, *M. rhomboideus anterior*; SHP, *M. scapulo-humeralis profundus posterior*; SRI, *M. serratus inferior*; SRM, *M. serratus medius*; SRS, *M. serratus superior*; SSC, *M. subscapularis*; STR, *M. sternoradialis*; tp, tympanic capsule; TRI, *M. triceps brachii long head*; TRI', *M. triceps brachii outer head*; TRI'', *M. triceps brachii inner head*; u, unidentified pectoral girdle muscle.

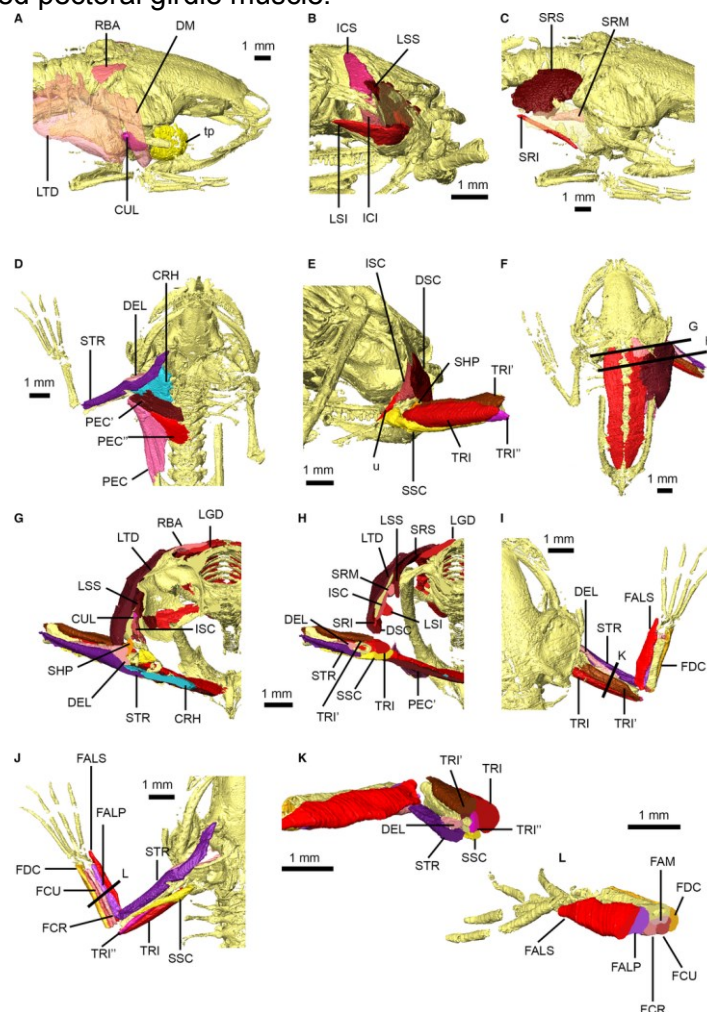


Fig. 7 Attachment sites for pectoral and forelimb musculature of *Xenopus laevis*. Skull shown in right posterolateral view (A). Right suprascapula and scapula shown in lateral (B) and medial (C) views. Close-up of pectoral and forelimb skeleton in right posterolateral view (D) and right ventrolateral view (E). Muscle attachment sites are identified using lowercase abbreviations. Abbreviations: crh, attachment of *M. coracobromalis*; cul, attachment of *M. cucullaris*; del, attachment of *M. deltoideus*; dsc, attachment of *M. dorsalis scapulae*; ici, attachment of *M. intertransversarius capitis inferior*; ics, attachment of *M. intertransversarius capitis superior*; isc, attachment of *M. interscapularis*; lsi, attachment of *M. levator scapulae inferior*; lss, attachment of *M. levator scapulae superior*; ltd, attachment of *M. latissimus dorsi*; pec, attachment of *M. pectoralis pars abdominalis*; pec', attachment of *M. pectoralis pars anterior sternalis*; pec'', attachment of *M. pectoralis pars posterior sternalis*; rba, attachment of *M. rhomboideus anterior*; shp, attachment of *M. scapulo-humeralis profundus posterior*; sri, attachment of *M. serratus inferior*; srm, attachment of *M. serratus medius*; srs, attachment of *M. serratus superior*; ssc, attachment of *M. subscapularis*; str, attachment of *M. sternoradialis*; tri, attachment of *M. triceps brachii long head*; tri', attachment of *M. triceps brachii outer head*; tri'', attachment of *M. triceps brachii inner head*.

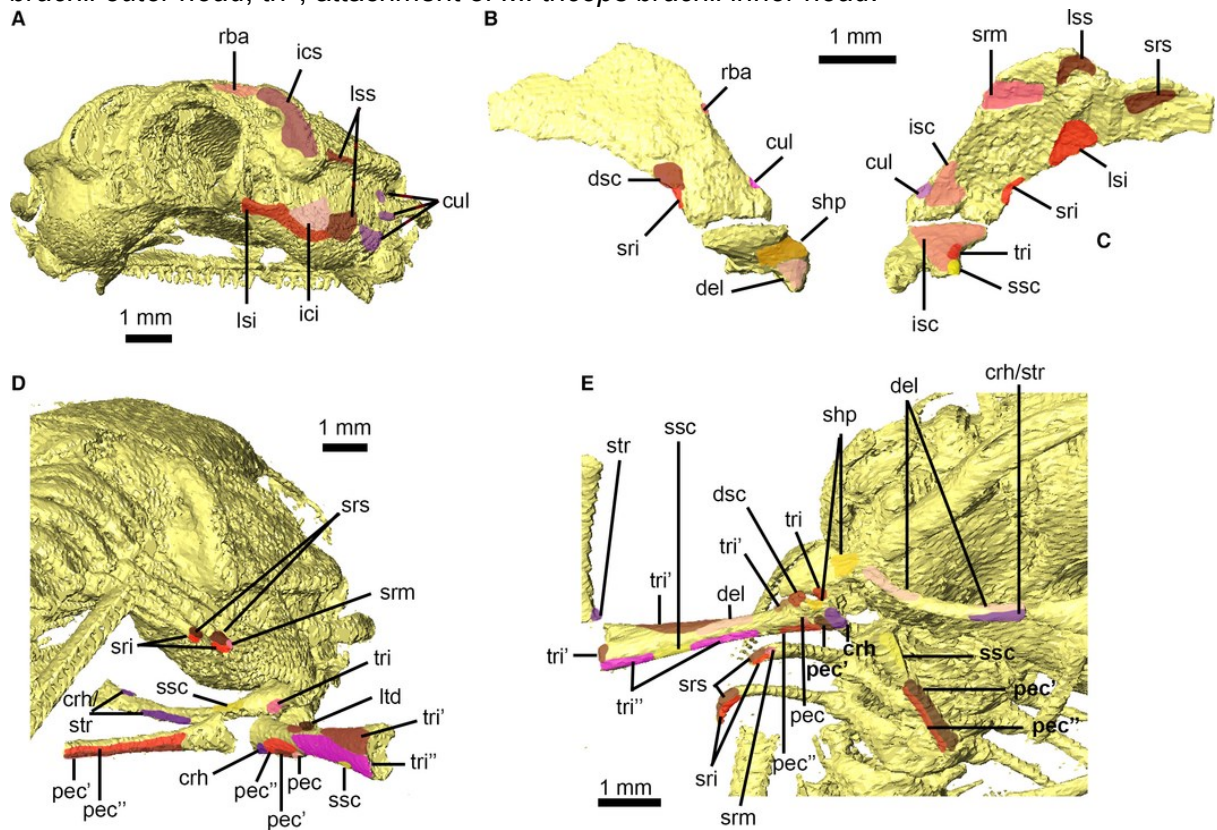


Fig. 8 Pelvic and thigh musculature of *Xenopus laevis*. Pelvic musculature in right dorsolateral (A) and ventral (B) views with the ligamentous plate removed. Superficial (C, D) and deep (E, F) thigh muscles in dorsal (C, E) and ventral (D, F) views. Dorsal view of specimen (G) showing location of cross-sections through the pelvis (H) and thigh (I – K). Muscles are identified using uppercase abbreviations; non-muscle structures are identified using lowercase abbreviations. Abbreviations: ADD, *M. adductor magnus, dorsal head*; ADL, *M. adductor longus*; ADV, *M. adductor magnus, ventral head*; CGI, *M. coccygeoiliacus*; CR, *M. cruralis*; GLM, *M. gluteus magnus*; GMA, *M. gracilis major*; GMI, *M. gracilis minor*; GML, *M. gemellus*; IE, *M. iliacus externus, superficial layer*; IE', *M. iliacus externus, middle layer*; IE'', *M. iliacus externus, extra middle layer*; IE''', *M. iliacus externus, deep layer*; IFB, *M. iliofibularis*; IFM, *M. iliofemoralis*; II, *M. iliacus internus*; IL, *M. iliolumbaris*; LGD, *M. longissimus dorsii*; Ip, ligamentous plate; OBE, *M. obturator externus*; OBI, *M. obturator internus*; PT, *M. pectineus*; PY, *M. pyramidalis*; SA, *M. sartorius*; SM, *M. semimembranosus*; ST, *M. semitendinosus*; TFL, *M. tensor fascia latae*.

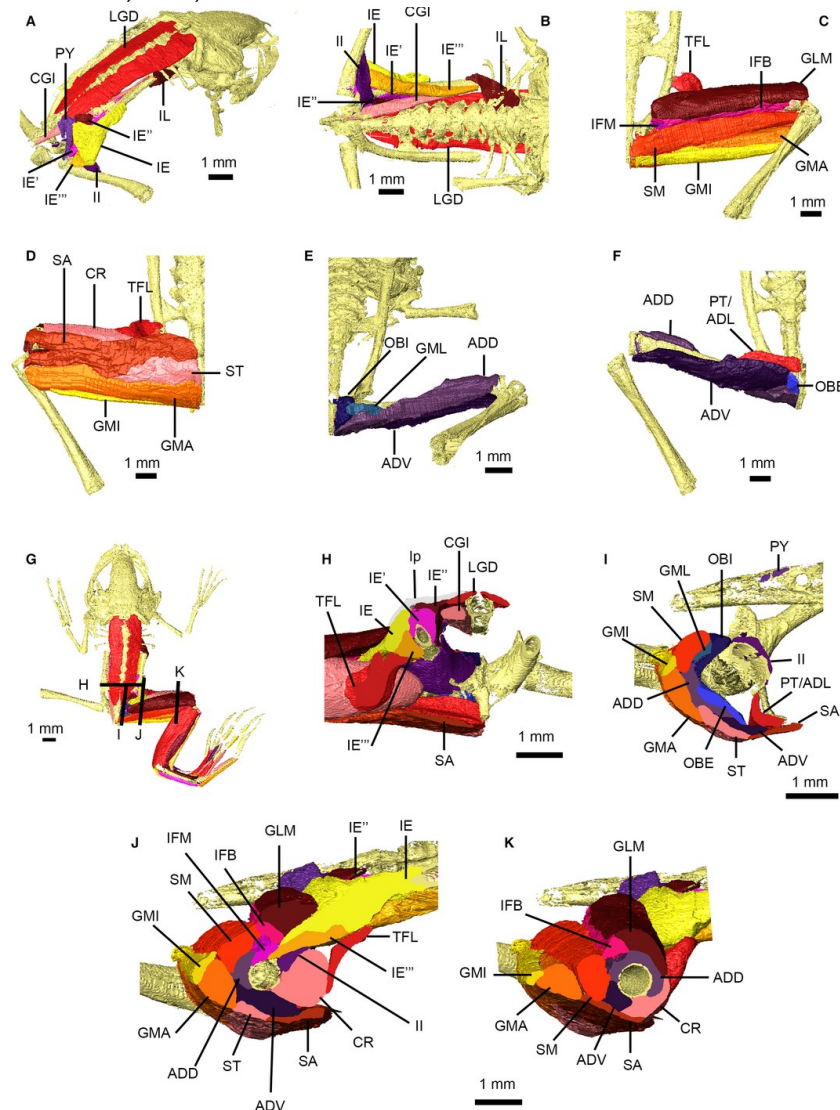


Fig. 9 Attachment sites for pelvic and thigh musculature of *Xenopus laevis*. Right ilium/pubis/ischium and urostyle in lateral view (A) and right ilium in medial view (B). Right femur in dorsal (C) and ventral (D) views. Muscle attachment sites are identified using lowercase abbreviations. Abbreviations: add, attachment of *M. adductor magnus*, dorsal head; adl, attachment of *M. adductor longus*; adv, attachment of *M. adductor magnus*, ventral head; cgi, attachment of *M. coccygeiliacus*; cr, attachment of *M. cruralis*; glm, attachment of *M. glutaeus magnus*; gma, attachment of *M. gracilis major*; gmi, attachment of *M. gracilis minor*; gml, attachment of *M. gemellus*; ie, attachment of *M. iliacus externus*, superficial layer; ie', attachment of *M. iliacus externus*, middle layer; ie'', attachment of *M. iliacus externus*, extra middle layer; ie''', attachment of *M. iliacus externus*, deep layer; ifb, attachment of *M. iliofibularis*; ifm, attachment of *M. iliofemoralis*; ii, attachment of *M. iliocostalis*; il, attachment of *M. iliolumbaris*; obe, attachment of *M. obturator externus*; obi, attachment of *M. obturator internus*; pt, attachment of *M. pectineus*; py, attachment of *M. pyramidalis*; sa, attachment of *M. sartorius*; sm, attachment of *M. semimembranosus*; st, attachment of *M. semitendinosus*.

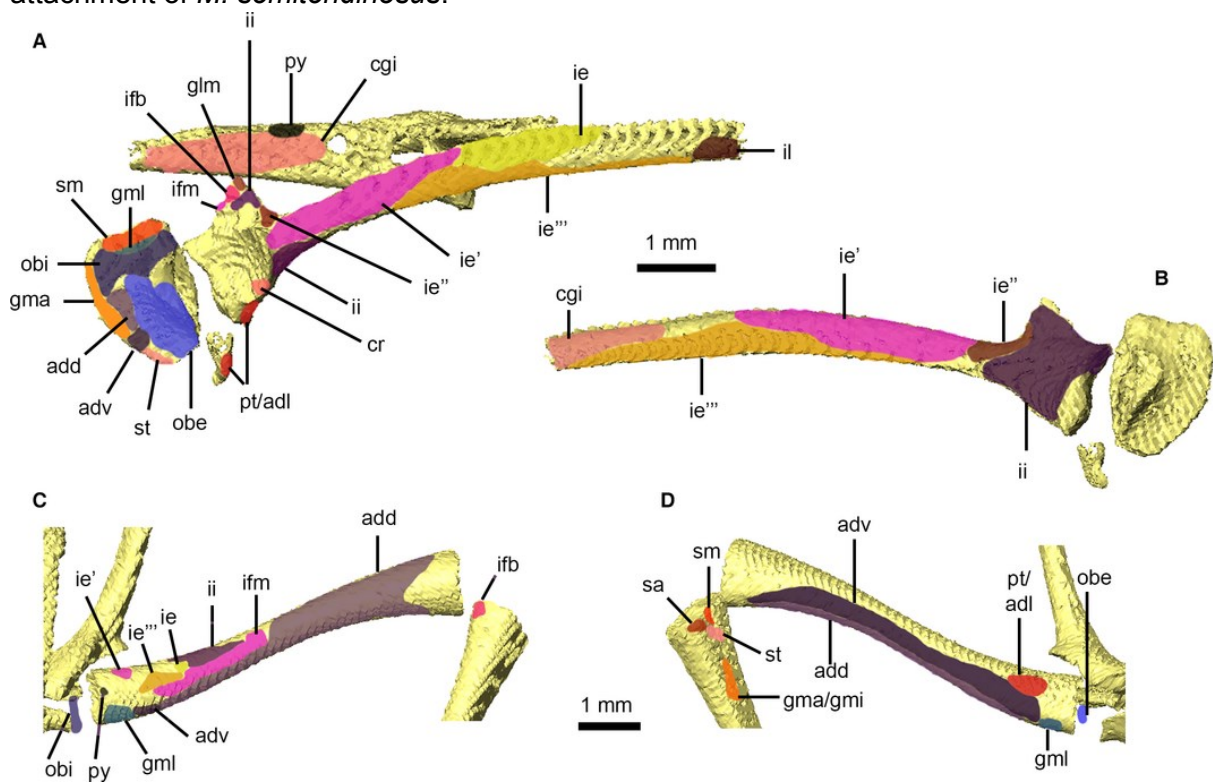


Fig. 10 Shank, tarsus and foot musculature of *Xenopus laevis*. Right shank and tarsal musculature in dorsal (A) and ventral (B) views. Dorsal view of specimen (C) showing location of cross-sections through the shank (D, E) and tarsus (F). Right foot musculature in dorsal (G) and ventral (H) views. Attachment sites on the right tibiofibula in dorsal (I) and ventral (J) views, and for the right tarsus in dorsal (K) and ventral (L) views. Main muscles are identified using uppercase abbreviations; muscle attachment sites and non-muscle structures are identified using lowercase abbreviations. Abbreviations: ABD 5, *M. abductor brevis dorsalis digiti V*; abd 5, attachment of *M. abductor brevis dorsalis digiti V*; ABDH, *M. abductor brevis dorsalis hallucis*; abdh, attachment of *M. abductor brevis dorsalis hallucis*; ABP 5, *M. abductor brevis plantaris digiti V*; ABPH, *M. abductor brevis plantaris hallucis*; EBM 2, *M. extensor brevis medius digiti II*; ebm 2, attachment of *M. extensor brevis medius digiti II*; EBP 2 - 4, *M. extensor brevis profundus digiti II - IV*; EBS 1, *M. extensor brevis superficialis hallucis*; ebs 1, attachment of *M. extensor brevis superficialis hallucis*; EBS 2 - 4, *M. extensor brevis superficialis digiti II - IV*; ebs 2 - 4, attachment of *M. extensor brevis superficialis digiti II - IV*; ECD, *M. extensor cruris brevis*; ecd, attachment of *M. extensor cruris brevis*; EDCL, *M. extensor digitorum communis longus*; FDBS, *M. flexor digitorum brevis superficialis*; IPD, *M. interphalangeales digitorum III- V*; IT, *M. intertarsalis*; it, attachment of *M. intertarsalis*; LUM, *M. lumbricales*; PE, *M. peroneus*; pe, attachment of *M. peroneus*; PL, *M. plantaris longus*; pl, attachment of *M. plantaris longus*; plt, plantaris tendon; PP, *M. plantaris profundus*; pp, attachment of *M. plantaris profundus*; TA, *M. tarsalis anticus*; ta, attachment of *M. tarsalis anticus*; TAB, *M. tibialis anticus brevis*; tab, attachment of *M. tibialis anticus brevis*; TAL, *M. tibialis anticus longus*; tal, attachment of *M. tibialis anticus longus*; TBP, *M. tibialis posticus*; tbp, attachment of *M. tibialis posticus*; TP, *M. tarsalis posticus*; tp, attachment of *M. tarsalis posticus*; u, unknown foot muscles.

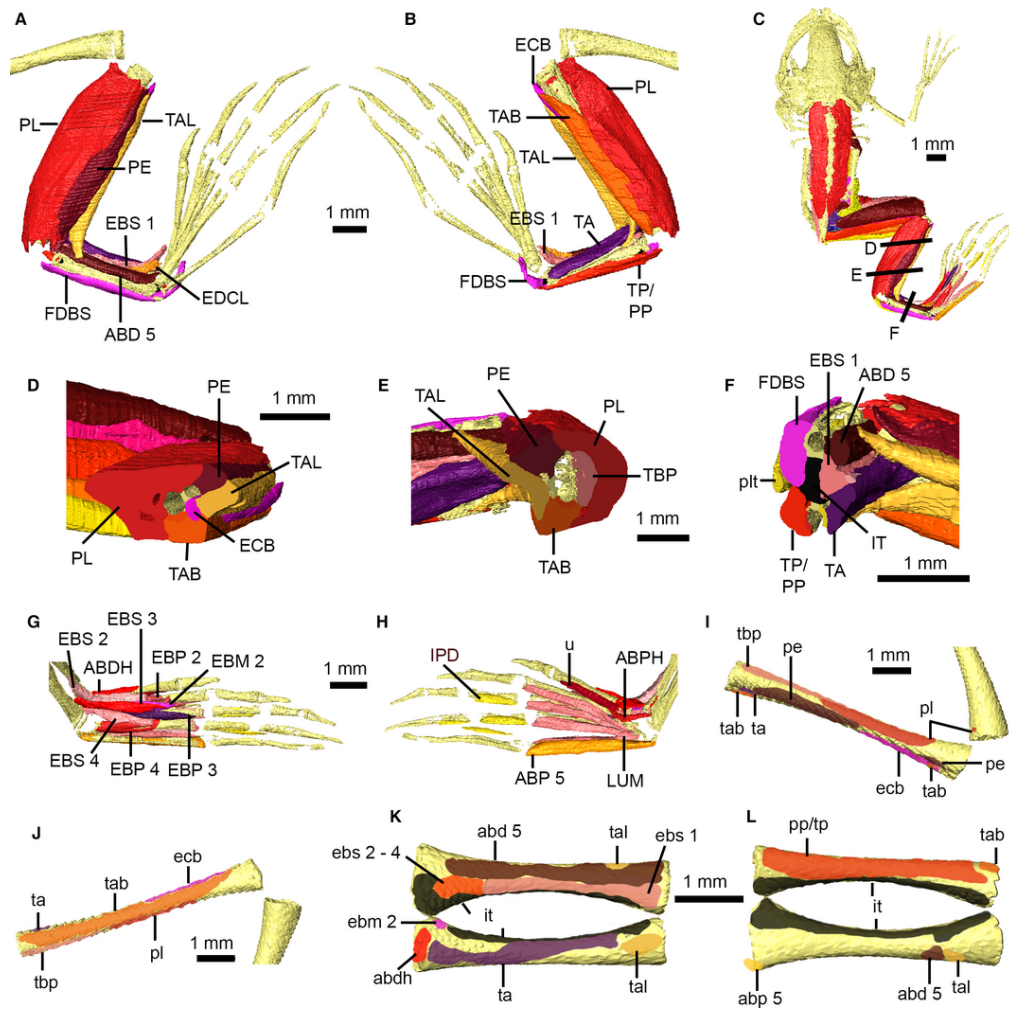


Fig. 11 Nervous system of *Xenopus laevis*. Brain in dorsal (A, C) and left lateral (B, D) views, with brain transparent in C and D to illustrate internal ventricles and pineal body. Cranial nerves in dorsal view (E), with eyes, nasal capsules, brain and spinal cord transparent. Left and right trigeminal nerves (F) in dorsal view. Peripheral nervous system in dorsal view (G), with brain, spinal cord and skeleton transparent (cranial nerves not shown). Abbreviations: caq, cerebral aqueduct; cbl, cerebellum; cbh, cerebral hemispheres; CN I - X, cranial nerves 1 - 10; dch, diencephalon; ft, filum terminale; gg, Gasserian ganglion; hyp, hypothalamus; ifr, infundibular recess; mmt, maxilla-mandibular trunk; mob, medulla oblongata; ncp, nasal capsules; opl, optic lobes; pn, pineal body; pnv, palatine nerve; S 1 - 10, spinal nerves 1 - 10; sc, spinal cord; v 1&2, first and second ventricles; v3, third ventricle; v4, fourth ventricle; vo, optic ventricles.

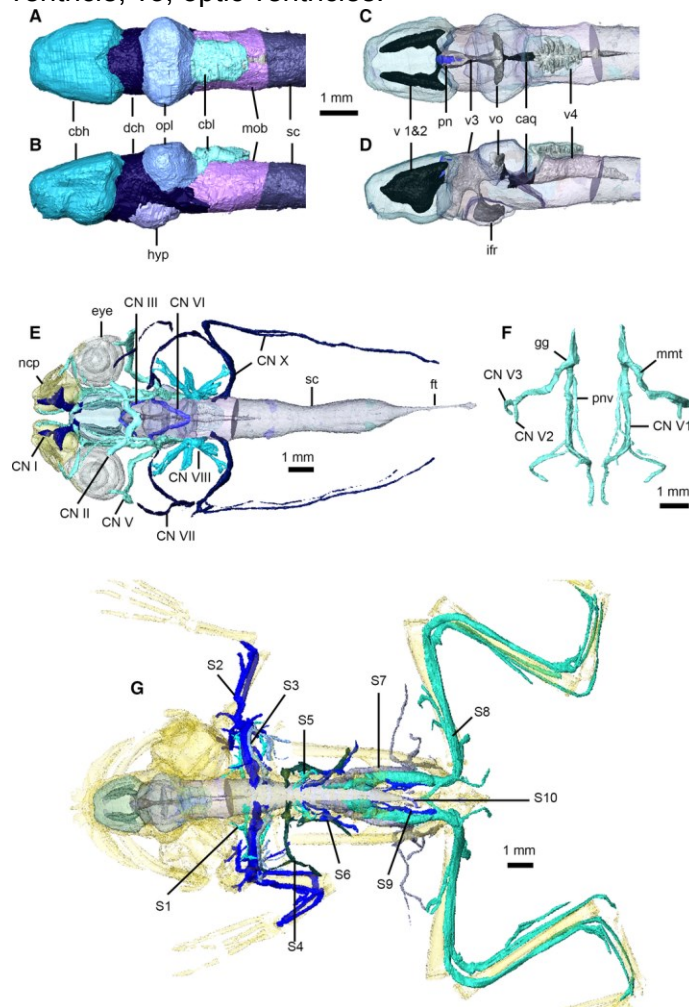


Fig. 12 Digestive, urogenital and respiratory systems of *Xenopus laevis*. Digestive and urogenital organs in ventral (A) and dorsal (B) views. Respiratory system in ventral view (C). Abbreviations: bld, bile and cystic ducts; dil, *M. dilator laryngis*; eso, esophagus; gal, gallbladder; imxg, intermaxillary glands; kid, kidney; liv, liver; lgin, large intestine and rectum; lng, lung; lyx, larynx; pan, pancreas; smin, small intestine; spl, spleen; sto, stomach; thd, thyroid gland; thm, thymus gland; tst, testes; urt, ureter.

